JGR Solid Earth

RESEARCH ARTICLE
10.1029/2021JB022742

Key Points:

- At room temperature, water has negligible effect on peak strength and the pressure of the brittle-ductile transition in Solnhofen limestone
- Water and elevated temperature together promote compaction and strain hardening and decrease the pressure of the brittle-ductile transition
- Water and thermal weakening are explained by water-enhanced fracturing and thermally enhanced glide and twinning

Supporting Information:

Supporting Information may be found in the online version of this article.

Correspondence to:

M. E. French,
mefrench@rice.edu

Citation:

French, M. E., Zhu, W., Xiao, X., Evans, B., & Prior, D. J. (2022). Thermally enhanced water weakening of the Solnhofen limestone. *Journal of Geophysical Research: Solid Earth*, *127*, e2021JB022742. https://doi.org/10.1029/2021JB022742

Received 1 JUL 2021
Accepted 24 FEB 2022

Thermally Enhanced Water Weakening of the Solnhofen Limestone

Melodie E. French[1], Wenlu Zhu[2], Xiaohui Xiao[3], Brian Evans[3], and David J. Prior[4]

[1]Department of Earth, Environmental and Planetary Sciences, Rice University, Houston, TX, USA, [2]Department of Geology, University of Maryland, College Park, MD, USA, [3]Department of Earth, Atmospheric and Planetary Sciences, Massachusetts Institute of Technology, Cambridge, MA, USA, [4]Department of Geology, University of Otago, Dunedin, New Zealand

Abstract We report the strength and deformation behavior of Solnhofen limestone across its brittle (localized) to ductile (distributed) transition. We conducted conventional triaxial compression tests on water-saturated and nominally dry cores of Solnhofen at temperatures up to 200°C and effective confining pressures up to 350 MPa to evaluate the roles of pore water and temperature on the deformation mechanisms of low-porosity limestone at conditions of the upper crust. The combined effects of water and temperature on deformation and strength of the limestone are complex and reflect the concurrent operation of microfracturing, which is enhanced by both pore water and temperature, crystal plasticity, which is enhanced by temperature but not pore water, and likely also dissolution which is enhanced by water but inhibited by temperature. At ambient temperature, water causes a small reduction in the yield strength and the strength in the ductile field, but has no measurable effect of the brittle peak strength or the effective pressure of the brittle to ductile transition. At elevated temperatures, water-saturated Solnhofen exhibits weakening in both the brittle and ductile fields up to 200 MPa effective pressure. In addition, the combined effects of pore water and temperature reduce the pressure of the brittle to ductile transition dramatically. We propose that under dry conditions temperature reduces the pressure of the brittle to ductile transition by enhancing crystal plasticity and under water-saturated conditions enhanced microcracking is responsible. At effective pressures greater than 200 MPa, ductile deformation becomes temperature strengthening indicating the onset of dissolution mediated deformation.

1. Introduction

Limestone occurs in systems that host natural hazards and nonconventional energy resources. As a result, the deformation of limestone may impact many important processes in the Earth. Many of the pelagic sediments subducted at convergent plate boundaries are carbonates (Barnes et al., 2010; Plank & Langmuir, 1998). It is, therefore, reasonable to posit that they may play a critical role in the strength and style of deformation along the subduction megathrust (e.g., Boulton et al., 2019; French & Condit, 2019; Rabinowitz et al., 2018). Although limestone has been proposed to contribute to the style of slip at some subduction zones (Dielforder et al., 2015; Leah et al., 2020), a comprehensive understanding of the contribution of limestone relative to other pelagic sedimentary rocks is lacking due to an incomplete understanding of limestone constitutive properties. The mode of deformation, including the degree to which deformation is strain weakening and localized or strain hardening and distributed, is particularly important for controlling the strength, distribution of deformation, and permeability structure of the upper crust and plate boundary fault zones. Although porous rocks, including carbonates, are shown to undergo a brittle to ductile transition due to pore collapse as a result of increasing pressure, there are few constraints on the roles of pore water and temperature on this transition (Jefferd et al., 2021; Nicolas et al., 2017). As a result, we still have limited ability to extrapolate laboratory data and predict the mode of deformation in the Earth.

Many studies have been conducted to understand the deformation behavior of limestone, including some of the earliest rock deformation experiments (Griggs et al., 1960; Heard, 1960; Turner et al., 1954). Previous studies have targeted the roles of pressure, temperature, pore fluids, porosity, and grain size on the constitutive behavior and deformation style of limestones and marbles over a wide range of conditions (e.g., Bakker et al., 2015; Baud, Zhu, & Wong, 2000; Brantut et al., 2014; Fredrich et al., 1989; Noël, Passelègue, & Violay, 2021; Rutter, 1972, 1974; Vajdova et al., 2004). These studies consistently show that the evolution of strength and volumetric strain across the brittle to ductile transition is qualitatively similar, but more complex, in calcite-rich rocks than in siliclastic rocks of similar porosity owing to the activation of twinning, dislocation glide, and pressure solution creep in calcite at low temperatures (Griggs et al., 1960; Turner et al., 1954). The pressure of the transition from brittle to ductile deformation decreases with increasing porosity in porous carbonates (Vajdova et al., 2004; Wong & Baud, 2012), which is phenomenologically similar to porous siliclastic rocks (Wong et al., 1997). However, whereas the transition in siliclastics is primarily controlled by microfracturing and cataclastic pore collapse, which are enhanced by both water and temperature, crystal-plastic mechanisms that are thermally activated but insensitive to pore water are thought to control to this transition in carbonates (Lisabeth & Zhu, 2015; Nicolas et al., 2016).

Under dry conditions, micromechanical models for limestone deformation show that the transition with increasing pressure from dilation and localization to compaction and distributed deformation is due to a transition from microcracking to pore collapse due to low-temperature plasticity (Baud, Zhu, et al., 2000). Application of this model has been successful in providing quantitative descriptions of strength and volumetric strain during deformation of dry limestone samples that have porosities of 0.03 and 0.15 (Nicolas et al., 2017). The few previous studies that have investigated the effects of water-saturated conditions and elevated temperatures on the deformation mechanisms and behavior of limestone have focused on relatively high porosity (∼14%–16%) samples (Brantut et al., 2014; Lisabeth & Zhu, 2015; Nicolas et al., 2016). Low-temperature plasticity is thermally activated so that elevated temperatures are expected to enhance plastic pore collapse, as illustrated by the reduction in the pressure of the transition from dilatant brittle deformation to compactive ductile deformation with increasing temperature in the Tavel limestone (Nicolas et al., 2016). However, pore water is not expected to affect pore collapse by crystal plasticity, but does enhance microcracking that can either lead to brittle fracture or pore collapse. In some cases, pore water also activates dissolution processes that promote compaction (Brantut et al., 2014; Lisabeth & Zhu, 2015). The result of these sometimes competing effects of temperature and pore water on the deformation and brittle to ductile transition of limestone are, therefore, challenging to predict. The complex effects of water are demonstrated by previous experiments showing that water has negligible effect on the strength of low-porosity marble (Rutter, 1974) and the peak strength of high-porosity limestone (Nicolas et al., 2016), but weakens the yield strength of high-porosity limestone (Nicolas et al., 2016).

We use rock deformation experiments to study the combined effects of aqueous pore fluids and temperature on the brittle to ductile transition of the Solnhofen limestone, a low-porosity limestone that has been studied extensively, primarily under dry conditions. We conducted conventional triaxial compression experiments at temperatures from 21°C to 200°C, and at effective pressures from 20 to 350 MPa. Most experiments were conducted under water-saturated conditions to determine the effects of temperature on the brittle to ductile transition of water-saturated Solnhofen limestone, and a small suite of experiments were conducted under dry conditions to evaluate the effects of pore water on strength. In addition to our own experiments, we compile published experimental data for the brittle to ductile transition in Solnhofen limestone to evaluate the combined roles of pore water and temperature on the transition.

2. Methods

2.1. Sample Description

The Upper Solnhofen limestone member is an extremely fine-grained (5–10 μm) lithographic limestone composed of 99.9% calcite (Barthel, 1970). It formed by the deposition of a fine-grained carbonate mud in a marine environment, which subsequently experienced diagenesis that resulted in an interlocking grain texture and low porosity (Munnecke et al., 2008). Because of its small grain size, homogeneous microstructure, and near-isotropic strength (Heard, 1960), the Solnhofen limestone has been used in many experimental studies. Our sample is of unknown origin, and was also studied by Fredrich et al. (1989).

We conducted deformation experiments on cylindrical cores of Solnhofen limestone with the axes of the cores normal to bedding. Each core was dried in an oven at 80°C for several days. Samples that were tested with pore water were then saturated with deionized water under vacuum for between 48 and 96 hr to ensure saturation of connected porosity and chemical equilibrium between the sample and pore fluid (e.g., Lisabeth & Zhu, 2015). Neglecting the minor amounts of impurities, the total porosity of our Solnhofen limestone sample is estimated to be 4.5% ± 0.4%, which was determined by comparing the masses of dried cores with the mass calculated for a core of equivalent volume composed of pure calcite. The effective porosity of our Solnhofen sample was determined to be 3.9% by comparing the masses of dried and water-saturated cores. These total and effective

Table 1
Summary of the Experimental Conditions and Mechanical Strength[a]

Sample ID	Pore fluid	T (°C)	$\sigma_3 - P_f$ (MPa)	σ_Y (MPa)	σ_P (MPa)	σ_F (MPa)	h (MPa)	m
Slf-10	H_2O	21	20	165	312	–	−15,810	−1.81
Slf-01	H_2O	21	50	255	360	–	−1,530	−0.90
Slf-11	H_2O	21	70	180	365	349	−760	−0.81
Slf-02	H_2O	21	100	234	404	399	−190	−0.62
Slf-09	H_2O	21	100	175	354	–	−50	0.01
Slf-05	H_2O	21	150	155	–	376	230	0.0
Slf-18	H_2O	21	150	230	–	433	709	−0.11
Slf-p17[b]	H_2O	21	150	250	–	451	290	−0.17
Slf-04	H_2O	21	250	107	–	361	1,270	0.24
Slf-07	H_2O	21	350	95	–	345	940	0.16
Slf-03	H_2O	50	50	231	348	–	−1,450	−0.79
Slf-16	H_2O	50	70	210	–	378	460	−0.29
Slf-12	H_2O	100	20	205	302	–	−17,370	−1.26
Slf-06	H_2O	100	50	173	334	327	−390	−0.54
Slf-15	H_2O	100	70	223	–	345	180	−0.25
Slf-08	H_2O	100	100	190	–	372	570	−0.01
Slf-p14[b]	H_2O	100	100	200	–	385	300	0.02
Slf-p18[b]	H_2O	100	200	175	–	411	780	0.11
Slf-13	H_2O	200	20	168	269	233	−670	−0.91
Slf-14	H_2O	200	20	170	264	236	−1,480	−0.59
Slf-17	H_2O	200	50	165	–	305	60	−0.08
Slf-p16[b]	H_2O	200	70	185	–	311	460	0.11
Slf-p15[b]	H_2O	200	150	160	–	396	900	0.12
Slf-p10[b]	H_2O	200	250	180	–	455	2,040	–
Slf-p12[b]	Ar	21	150	300	–	490	90	−0.21
Slf-p13[b]	Ar	100	100	280	–	424	380	−0.33
Slf-p19[b]	Ar	200	70	260	392	375	−210	−0.19
Slf-p20[b]	Ar	200	100	270	–	407	425	0.18

[a] $\sigma_3 - P_f$ is the effective confining pressure, σ_Y is the yield strength, σ_P is the peak strength, σ_F is the strength at four percent axial strain, h is the hardening coefficient, and m is the dilatancy coefficient. [b] Experiments conducted with the Paterson apparatus. All others were conducted using the Goetze apparatus.

porosities are within the range of samples previously studied experimentally (Baud, Zhu, et al., 2000; Renner & Rummel, 1996; Rutter, 1972).

2.2. Experiments

We conducted a suite of 28 conventional triaxial compression experiments on Solnhofen limestone cores at a constant axial strain rate of $\dot{\epsilon}_a = 10^{-5}\ \mathrm{s}^{-1}$ to total axial strains, ϵ_a, between 0.02 and 0.15 (Table 1; French et al., 2021). We use the convention that compressive stresses and shortening strains are positive and that σ_1 and σ_3 are the greatest and least compressive stresses, respectively. We present strength in terms of the differential stress $\sigma_d = \sigma_1 - \sigma_3$. Experiments were conducted at a constant externally controlled pore pressure (P_f) of 50 MPa, constant effective confining pressures ($\sigma_3 - P_f$) of 20–350 MPa, and constant temperatures from room temperature (21°C) to 200°C.

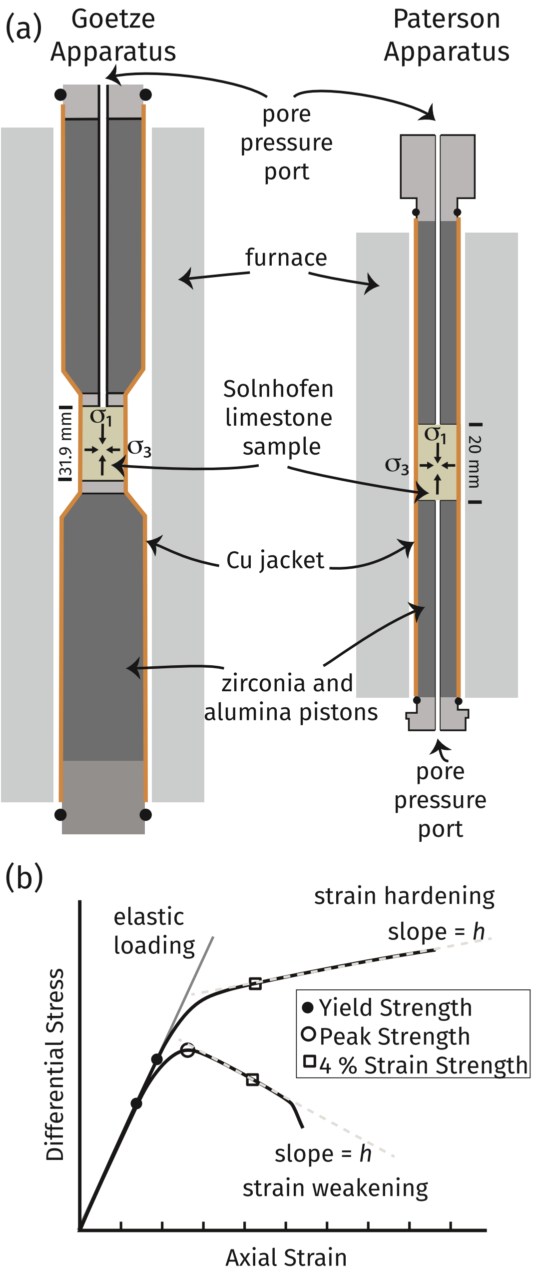

Figure 1. (a) Schematic diagrams of the Goetze and Paterson deformation apparatus. (b) Illustration of the measures of the yield strength (solid circle), peak strength (empty circle), strength at 4% axial strain (empty square), and hardening modulus, $h = \partial\sigma_d/\partial\epsilon_a$, for strain weakening and strain hardening mechanical behavior. The transition from strain weakening to strain hardening mechanical behavior also correlates with a transition from localized to distributed deformation and defines the brittle to ductile transition.

Most experiments (18) were conducted in the Goetze apparatus and 10 experiments were conducted in the Paterson apparatus, both located at the Massachusetts Institute of Technology (Figure 1a). At two sets conditions (21°C and 150 MPa effective pressure and 100°C and 100 MPa effective pressure), water-saturated experiments were conducted in both the Goetze and Paterson apparatus to confirm comparable mechanical data (Table 1). In both apparatus, all data were digitized and recorded at a sampling frequency of 1 Hz. All experiments conducted with the Goetze apparatus were conducted with Ar gas confining medium and deionized water pore fluid. For this apparatus, the axial piston is hydraulically driven and servo-controlled. The confining pressure is applied with a Haskell pump and pore pressure is applied and maintained with a servo-controlled piston screw pressure intensifier connected to one end of the sample. Temperature is applied and controlled with a two-zone wound internal furnace. Cores deformed in the Goetze apparatus are 15.85 mm in diameter and 31.90 mm in length. Displacement of the axial piston is measured with a linear variable differential transformer (LVDT) displacement transducer located external to the pressure vessel, and this measurement was corrected for elastic distortion of the apparatus. Axial force is measured with a gauge external to the vessel and was corrected for seal friction and divided by sample area to determine the axial stress, σ_1.

Experiments performed with the Paterson apparatus use Ar gas confining medium and either Ar gas (4 experiments) or deionized water (6 experiments) pore fluid. For the Paterson apparatus, the axial piston, confining pressure, and pore pressure are servo-controlled, and temperature is applied and controlled with a three-zone furnace internal to the pressure vessel. Experimental cores are 10.0 mm in diameter and 20.0 mm in length, and pore fluid pressure is applied and controlled independently at both sample ends. Displacement of the axial piston is measured with an LVDT located external to the pressure vessel, and this measurement was corrected for elastic distortion of the apparatus. Axial force is measured with a gauge internal to the vessel and divided by sample area to determine the differential stress, σ_d.

In both systems, cores were jacketed with a thin-walled (0.3 mm) annealed copper tubing and data are not corrected for the strength of the jackets. We used the calculations of copper jacket strength by Higgs (1981) for the data of Handin and Hager (1958), which indicates that at 5% axial strain our jackets should support 15 MPa differential stress at room temperature and 12 MPa at 200°C, which is small (~2%–3%) compared to the strength of the Solnhofen limestone. Samples were loaded to deformation conditions by first applying ~10 MPa of confining pressure, and then increasing the pore pressure to ~8–9 MPa. Next, confining and pore pressure were increased simultaneously to 60 and 50 MPa, respectively, and confining pressure and temperature were then increased to the final deformation conditions. Samples equilibrated at experimental conditions for at least two hours prior to triaxial deformation. The reported strength has not been corrected for changes in cross-sectional area during sample barreling or faulting.

In both deformation systems, LVDTs measured displacement of the pore fluid pressure intensifier pistons as water was added or removed to the sample to maintain constant pore pressure. Sample volume change, ΔV, was measured by multiplying the displacement of the pore pressure intensifier pistons by their cross-sectional areas without taking into account thermal gradients between the sample and intensifier (Fischer & Paterson, 1989). Volumetric strain of the cores was calculated by dividing volume change by the initial core volume ($\epsilon_V = \Delta V/V$), where positive ϵ_V corresponds to compaction. The measure of volume change is useful for determining trends in evolution with increasing axial strain.

Table 2
Summary of Permeability Test Conditions and Measurements[a]

Sample ID	Pore fluid	$\sigma_3 - P_f$ (MPa)	T (°C)	Period (s)	# Measurements	Avg permeability (m^2)	Std dev (m^2)
Slfp-06	Ar	140	21	10, 20, 25	6	4.8×10^{-18}	0.3×10^{-18}
Slfp-08[a]	Ar	100	21	10	6	1.2×10^{-18}	0.2×10^{-18}
Slfp-08[a]	Ar	150	21	25, 50	6	1.0×10^{-18}	0.2×10^{-18}
Slfp-10	H_2O	250	200	50, 100	9	3.2×10^{-19}	0.4×10^{-19}
Slfp-20	Ar	100	200	50, 100	6	8.0×10^{-19}	0.2×10^{-19}

[a] Permeability was measured using the pore pressure oscillation technique with peak-to-peak wave amplitude of 0.4 MPa and a period given in this table. The average and standard deviation of the total number of measurements for each sample and condition are provided.

However, because the pore volume reservoirs are large in comparison to sample volume change and subject to thermal fluctuations in the room, the resolution is not sufficient for determining the stress at the onset of dilation (C') or shear enhanced compaction (C^*).

2.3. Experimental Drainage Conditions

We measured the permeability of five cores (Table 2) and use the results to confirm that the cores were "drained" during the experiments, meaning that pore fluid pressure within the sample remains approximately constant because fluid diffusion occurs fast enough to keep pace with pore volume changes. For three of the cores, permeability was measured under isotropic stress states only, and for two of the cores permeability was measured during triaxial compression and their mechanical data are reported (Table 1 and Figure 3). We used the pore pressure oscillation method in the Paterson apparatus on four dry cores and one water-saturated core under effective confining pressures between 100 and 250 MPa and at room temperature and 200°C (Table 2). We used a peak-to-peak oscillation amplitude of 0.4 MPa and tested at least two oscillation frequencies for each sample, finding no dependence on frequency. The permeability of our Solnhofen limestone sample is approximately one order of magnitude higher than that of Fischer and Paterson (1992), although direct comparison is challenging because they subjected their cores to high effective pressures of 250 MPa before any permeability measurements were made. Rashid et al. (2015) measured the permeability of 42 samples of Solnhofen limestone, and demonstrated that, even at a porosity of ~0.05, permeability of different samples spans 3 orders of magnitude from 10^{-20} to 10^{-17} m^2. Thus, the permeability of our sample and determination of sample drainage conditions cannot be easily extrapolated to studies of other Solnhofen limestone samples.

In the two tests during which permeability was measured during axial compression, we find that permeability initially decreases to approximately 3×10^{-20} m^2 within the first 2%–3% axial strain (Figure 2). The permeability of the water-saturated sample was not measured beyond this strain, but the permeability of the dry sample then gradually increased with increasing strain. Fischer and Paterson (1992) documented a similar evolution of permeability with strain during triaxial compression of dry Solnhofen limestone.

To estimate whether the cores remain drained during deformation experiments, we use the permeability measurements to calculate the ratio of the timescale of fluid diffusion, t_d, to the timescale of deformation, t_{def} ($N = t_d/t_{def}$; e.g., Duda & Renner, 2012; Fischer & Paterson, 1989). When $N \leq 1$, the system is considered drained. We approximate t_{def} as the time required to accommodate a ~1% increment of axial strain (Fischer & Paterson, 1989), which for our strain rate of 10^{-5} s^{-1} results in $t_{def} = 1{,}000$ s. The order of magnitude timescale of fluid diffusion is often approximated by $t_d = l^2/D$, where l is the length scale of diffusion and D is the hydraulic diffusivity (Carslaw et al., 1959). For samples deformed in the Goetze apparatus, l is 31.9 mm, and for those deformed in the Paterson apparatus, which has a double-ended pore pressure system, l is 10 mm. Hydraulic diffusivity is given by $D^{-1} = \eta(n_i(\beta_f - \beta_m) + \beta_r - \beta_m)/k$, where k is permeability, η is the dynamic viscosity of the pore fluid, n_i is interconnected porosity, and β_f, β_m, and β_r, are the compressibilities of the pore fluid, mineral constituents, and rock, respectively. We estimate $\beta_r = 2 \times 10^{-11}$ Pa^{-1} from hydrostatic loading of our samples and Schubnel et al. (2005), $\beta_m = 7.7 \times 10^{-12}$ Pa^{-1} for calcite, and $n_i = 0.039$.

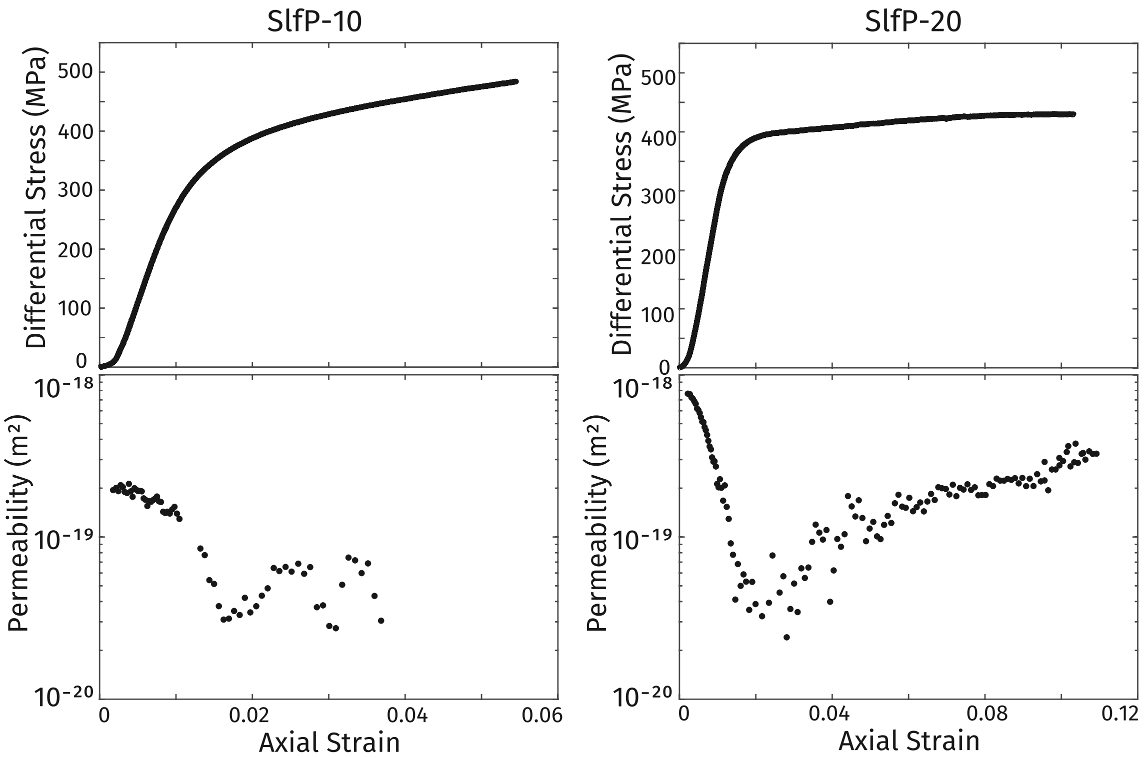

Figure 2. The evolution of differential stress and permeability during triaxial compression experiments Slfp-10 under water-saturated conditions, 250 MPa confining pressure, and 200°C and Slfp-20 under dry conditions, 100 MPa confining pressure, and 200°C (Table 2).

We calculate the timescale of fluid diffusion and N for each of our tests using the permeability measurements as constraints (Table 3). To estimate a minimum bound on permeability, we assume that the permeability is unlikely to be reduced by a full order of magnitude during triaxial deformation, as neither we nor Fischer and Paterson (1992) observed an order of magnitude reduction during deformation. Accordingly, we assume that $k \approx 10^{-19}$ m^2 is an appropriate lower bound for experiments conducted at room temperature and that $k \approx 3 \times 10^{-20}$ m^2 is a lower bound for experiments conducted at 100°C and 200°C independent of effective confining pressure. These values

Table 3
Estimates of Sample Drainage for Different Pore Fluids and Temperatures

Fluid	T (°C)	l[a] (mm)	k[b] (m^2)	η (Pa s)	β_f (Pa^{-1})	D (m^2/s)	t_d (s)	N	k_{crit}[c] (m^2)
H_2O	21	31.9	1×10^{-19}	1.0×10^{-3}	3.9×10^{-10}	3.7×10^{-6}	277	0.28	2.8×10^{-20}
H_2O	21	10	1×10^{-19}	1.0×10^{-3}	3.9×10^{-10}	3.7×10^{-6}	27	0.03	2.7×10^{-21}
H_2O	50	31.9	1×10^{-19}	5.5×10^{-4}	3.8×10^{-10}	6.8×10^{-6}	150	0.15	1.5×10^{-20}
H_2O	100	31.9	3×10^{-20}	2.8×10^{-4}	4.1×10^{-10}	3.8×10^{-6}	265	0.27	8.0×10^{-21}
H_2O	100	10	3×10^{-20}	2.8×10^{-4}	4.1×10^{-10}	3.8×10^{-6}	26	0.03	7.8×10^{-22}
H_2O	200	31.9	3×10^{-20}	1.0×10^{-4}	6.6×10^{-10}	7.9×10^{-6}	128	0.13	3.8×10^{-21}
H_2O	200	10	3×10^{-20}	1.0×10^{-4}	6.6×10^{-10}	7.9×10^{-6}	13	0.01	3.8×10^{-22}
Ar	21	10	1×10^{-19}	4.7×10^{-5}	8.6×10^{-11}	1.4×10^{-4}	1	0.002	7.1×10^{-23}
Ar	100	10	3×10^{-20}	4.5×10^{-5}	7.5×10^{-11}	4.5×10^{-5}	2	0.002	6.7×10^{-23}
Ar	200	10	3×10^{-20}	4.3×10^{-5}	6.4×10^{-11}	4.8×10^{-5}	2	0.002	6.2×10^{-23}

[a] l of 31.9 and 10 mm correspond to the Goetze and Paterson apparatus, respectively. [b] A lower bound estimate of permeability at the given fluid conditions and temperature. [c] The critical permeability, below which deformation would become undrained ($N = 1$).

may underestimate permeability at lower effective confining pressures than those of the permeability experiments. We take into account the appropriate fluid viscosity and compressibility at 50 MPa pore pressure, the experimental temperature, and the fluid diffusion length scale for each apparatus.

We find that our experiments can be considered drained during deformation at the experimental conditions (Table 3). In cases where either strain rate is locally high, such as during fracture formation, or pore compaction at the highest effective pressures reduces permeability, deformation may become undrained and we evaluate these cases in the discussion of the results. For the experimental conditions, we also calculate the sample permeability that would result in a transition to undrained deformation ($N = 1$) and report them in Table 2.

2.4. Microscopy

Thin sections were prepared from deformed samples and analyzed using a combination of polarized light microscopy and scanning electron microscopy (SEM). All thin sections were prepared parallel to the core axes and normal to any visible through-going shear fractures. Entire thin sections were scanned under plane- and cross-polarized light and used to document mesoscale transgranular fractures and distributed deformation. Given the extremely fine grain size of the Solnhofen, the grain scale deformation is not observable using polarized light microscopy and was documented with SEM. Back-scattered electron images were collected at a voltage of 20 kV and secondary electron (SE) images were collected at a voltage of 15 kV (Lloyd, 1985). In addition, electron back-scattered diffraction (EBSD) data were collected for sample Slf-02 using a CamScan X500 Crystal Probe, with a thermoionic field emission gun and FASTRACK stage (Table 1; Prior et al., 1999; Seward et al., 2002). Measurements were made at an accelerating voltage of 20 kV and beam current of 10 nA. The scan area was 120 × 100 μm with a step size of 0.2 μm (Lloyd, 1985). The thin section was polished with a diamond paste and colloidal silica polishing, and then covered with a thin coat of carbon.

3. Results

We describe the mechanical behavior and resulting structures of the Solnhofen limestone. In the presentation and analysis of results, we include the strength of Solnhofen reported by Fredrich et al. (1989; Table 4), because they tested the same sample of Solnhofen limestone at the same strain rate ($10^{-5}\ s^{-1}$) using the Goetze deformation apparatus. Thus, their data are directly comparable to ours.

3.1. Mechanical Data

Under water-saturated conditions, increasing pressure results in a transition from strain weakening to strain hardening behavior (Figure 3), as previously shown under dry conditions (Baud, Zhu, et al., 2000; Fredrich et al., 1989). At room temperature and water-saturated conditions, this transition occurs at approximately 100 MPa and with increasing temperature the transition shifts to lower pressures, occurring between 50 and 70 MPa at 100°C and at approximately 50 MPa at 200°C.

We characterize the yield strength, σ_Y, as the differential stress at which the strain hardening portion of the stress-strain curve deviates from linear and include in our comparison the data of (Fredrich et al., 1989) for the yield strength under dry conditions and at room temperature (Figures 1b and 3). This measure of yield strength exhibits significant scatter, but two general trends are evident. In general, σ_Y is pressure independent under water-saturated and dry conditions (Figures 4a and 4c). In addition, pore water does lower the yield strength relative to dry conditions. There is no measurable dependence of σ_Y on temperature under water-saturated or dry conditions. Comparison of pairs of experiments on the Goetze and Paterson apparatus (Slf-18 and Slf-p17 at 21°C and 150 MPa effective pressure and Slf-08 and Slf-p14 at 100°C and 150 MPa effective pressure) yield strengths are within 8% of one another which is similar to the variability between tests on the same apparatus.

We quantify the post-yield strength as the peak differential stress (σ_P) for samples that strain weaken, and include the data of (Fredrich et al., 1989) for peak strength under dry conditions and room temperature (Figures 1b and 3). To characterize the strength of both strain hardening and strain weakening samples at relatively high strain, we also quantify the differential stress at 4% axial strain (σ_F) for all samples that reached $\epsilon_a = 0.04$ (Figures 4b and 4d). Unlike σ_Y, σ_P increases with increasing pressure under all conditions tested, is temperature weakening under water-saturated conditions, and is not clearly affected by the presence of pore water at room temperature.

Table 4
Data Compiled From Previous Studies

Sample ID	Pore fluid	T (°C)	Pc' (MPa)	σ_Y (MPa)	σ_P (MPa)	σ_F (MPa)	h (MPa)	m
Frederich et al. (1990)[a]								
SL4	Dry	Room	50	–	376	–	–	–
SL5	Dry	Room	85	278	385	–	–	–
SL6	Dry	Room	70	255	370	–	–	–
SL7	Dry	Room	60	261	368	–	–	–
SL8	Dry	Room	300	178	–	–	–	–
SL9	Dry	Room	10	268	323	–	–	–
SL10	Dry	Room	5	280	323	–	–	–
SL11	Dry	Room	0	287	320	–	–	–
Baud, Schubnel, et al. (2000) and Baud, Zhu, et al. (2000)[b]								
	Dry	Room	10	–	326	–	–	–
	Dry	Room	25	–	360	–	–	–
	Dry	Room	35	–	409	–	–	–
	Dry	Room	50	–	428	–	–	–
	Dry	Room	200	–	–	525	–	–
	Dry	Room	300	–	–	560	–	–
	Dry	Room	350	–	–	575	–	–
Renner and Rummel (1996)[c]								
slII1/10	Dry	Room	50	–	–		−5,050	−0.98
slII2/9	Dry	Room	65	–	–		−5,400	−0.65
slII2/4	Dry	Room	80	–	–		−690	−0.55
slII2/1	Dry	Room	100	–	–		−280	−0.58
slII2/5	Dry	Room	120	–	–		190	−0.26
slII2/6	Dry	Room	150	–	–		470	−0.16
slII2/7	Dry	Room	195	–	–		810	−0.04

[a] Data are presented in Figures 4c and 4d. [b] Data are presented in Figure 4d. [c] Data are presented in Figures 5c and 5d.

Under water-saturated conditions, σ_F increases with pressure until 150 MPa (Figure 4b). At room temperature, σ_F then decreases with increasing pressure, but at elevated temperatures, σ_F remains pressure strengthening. As a result, at pressures up to ∼150 MPa, σ_F is temperature weakening under water-saturated conditions, but at higher pressures transitions to temperature strengthening. Comparison of pairs of experiments on the Goetze and Paterson apparatus (Slf-18 and Slf-p17 at 21°C and 150 MPa effective pressure and Slf-08 and Slf-p14 at 100°C and 150 MPa effective pressure) σ_F is within 4% of one another which is similar to the variability between tests on the same apparatus. We plot the data of Baud, Zhu, et al. (2000) for σ_F at room temperature and under dry conditions to show that dry Solnhofen limestone is pressure strengthening over the same range of effective pressures that our water-saturated Solnhofen limestone is pressure weakening (Figure 4d and Table 4). Although we conducted fewer experiments under dry conditions, our results consistently show that σ_F is greater under dry than water-saturated conditions at the same pressure and temperature (Figure 3).

Among water-saturated samples that strain weaken, rapid uncontrolled stress drops only occur at 20 MPa effective confining pressure and temperatures of 21°C and 100°C, and strain weakening curves in these experiments are dominated by apparatus stiffness (Figure 3). At higher pressures and/or temperatures, strain weakening samples have a linear weakening slope that is sometimes followed by a second phase of accelerated dynamic weakening controlled by apparatus stiffness. Samples that strain harden generally exhibit linear strengthening at effective pressures up to 150 MPa within the strain interval that we observed in our experiments; however,

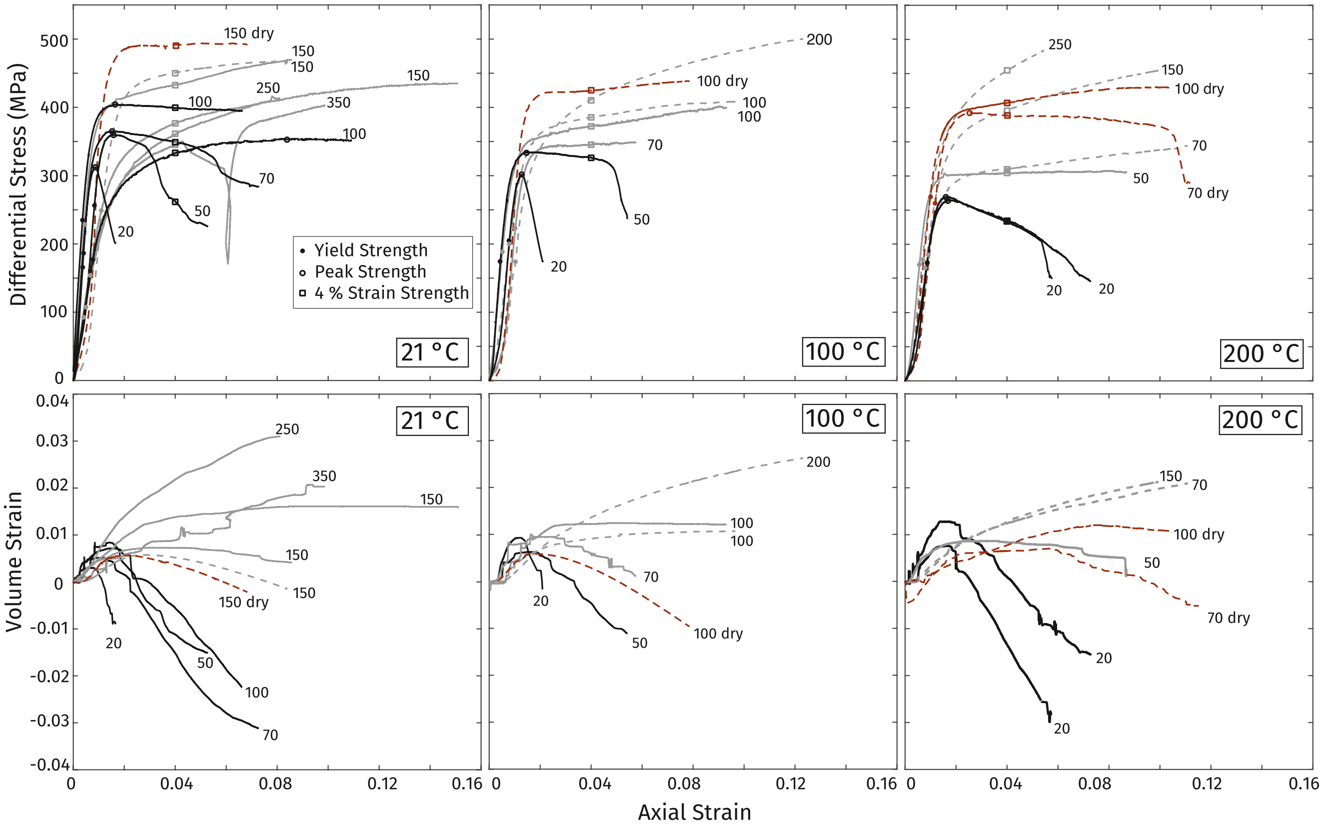

Figure 3. The evolution of differential stress (top) and volume strain (bottom) with increasing axial strain at different temperatures. Samples deformed with deionized water as the pore fluid are indicated in black if they are strain weakening and gray if they are strain hardening, samples deformed with Ar pore fluid are shown in red, samples deformed in the Goetze apparatus are shown with solid lines and those deformed with the Paterson apparatus are shown in dashed lines. Numbers indicate effective confining pressure ($\sigma_3 - P_f$) in MPa (Table 1). The weakening and recovery of the sample deformation at room temperature and 350 MPa corresponds to an uncontrolled drop in confining pressure that was subsequently recovered.

at the highest effective pressures (200–350 MPa) strain hardening is non-linear. We use the hardening coefficient, $h = \partial\sigma_d/\partial\epsilon_a$, to quantify the strain-dependent strength, where positive values of h indicate hardening (e.g., Fredrich et al., 1989, 1990; Renner & Rummel, 1996). At the highest effective pressures, which exhibit a decreasing hardening coefficient with strain, we approximate a hardening coefficient with a linear fit to the data between 6% and 8% axial strain. Under water-saturated conditions, the hardening coefficients increase non-linearly with increasing pressure, and higher temperatures correlate with higher values of h and enhanced hardening (Figure 5a). For comparison, we show the data of Renner and Rummel (1996; Table 4), who reported hardening coefficients for dry Solnhofen limestone at room temperature (Figure 5b). Our experiment conducted at room temperature and under dry conditions falls within the trend established by Renner and Rummel (1996; Figures 5c and 5d). At room temperature, we find there is no measurable effect of pore water on the hardening coefficient (Figure 5c). Temperature does seem to cause an increase in the hardening coefficient, although data are limited and the apparent effect is smaller than under water-saturated conditions (Figure 5c).

In addition to being weaker, water-saturated limestone consistently exhibits greater compaction than dry limestone deformed at the same conditions (Figure 3), which can be illustrated in plots of effective mean stress ($\sigma_m = \sigma_d/3 + \sigma_3 - P_f$) vs. volumetric strain (Figure 6 and Figure S1 in Supporting Information S1). To characterize the evolution of volumetric strain with ϵ_a (Figure 3), we use the dilatancy coefficient, $m = \partial\epsilon_V/\partial\epsilon_a$ where positive m indicates compaction (Figure 5b). As for the hardening coefficient, we approximate the dilatancy coefficient with a linear fit to the data between 6% and 8% axial strain. Under water-saturated conditions, the dilatancy coefficient increases non-linearly with increasing pressure, similar to the evolution of h. Like h, higher temperatures promote larger values of m (Figure 5b). Strain weakening always corresponds to dilatant deformation, and strain hardening usually correlates with compactional deformation (Figures 3 and 5). Experiments that exhibit strain hardening and dilatant deformation likely represent shear enhanced dilatancy (Baud, Zhu, et al., 2000). We also

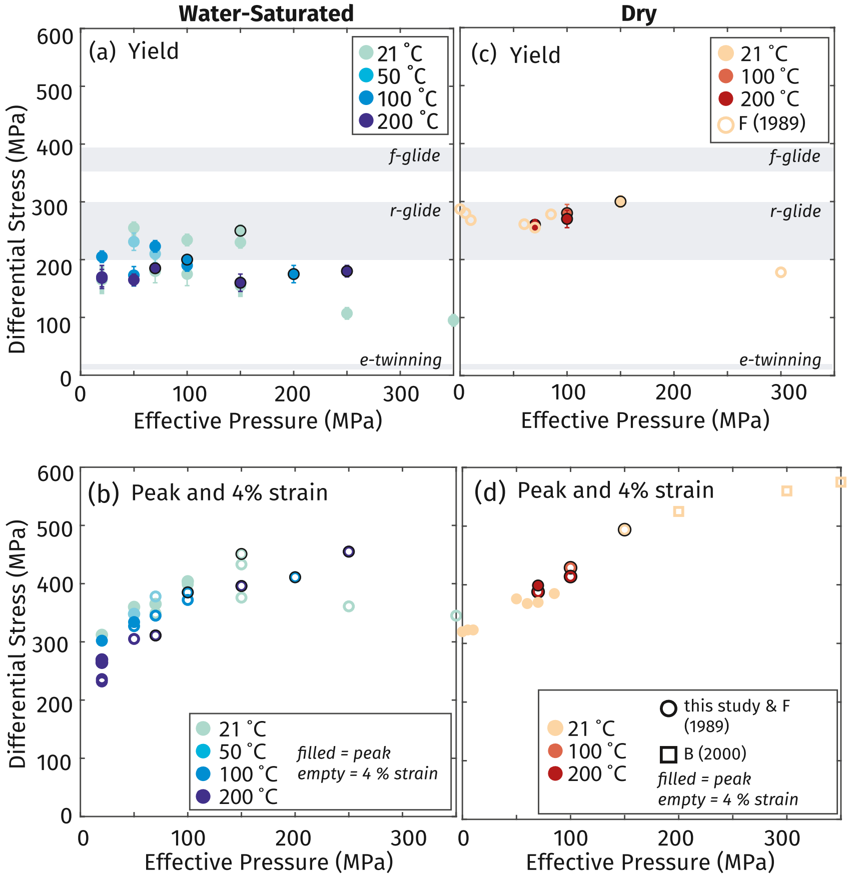

Figure 4. The (a) yield strength, σ_Y, and (b) peak strength, σ_P, (filled circles) and strength at 4% axial strain, σ_F (empty circles) for water-saturated samples at different effective confining pressures ($\sigma_3 - P_f$) and temperatures. The (c) yield strength, σ_Y, under dry conditions and at different temperatures from our data (filled circles) and Fredrich et al. (1989) (empty circles, F [1989, Table 4] and (d) peak strength, σ_P, and strength at 4% axial strain, σ_F for dry samples as a function of effective confining pressure at different temperatures. Peak strengths are from Fredrich et al. (1989 F, 1989), and strengths at 4% axial strain are from this study (empty circles) and Baud, Zhu, et al. (2000 empty squares, Table 4). The experiments of (Fredrich et al., 1989) did not reach 4% strain. σ_Y was determined by fitting a line to the data in Figure 3 between differential stresses of 75 and 150 MPa. Where the experimental data deviated from the linear fit was determined as yield. Error bars are visual estimates of the uncertainty in determining the deviation from a linear slope. Data from our experiments conducted with the Paterson apparatus are outlined in black and those conducted with the Goetze apparatus are without outlines. The differential stresses for yield on optimally orientated planes are shown for twinning along the *e*-plane $\left(\left\{01\bar{1}8\right\}\ \langle 40\bar{4}1\rangle\right)$, glide of the *r*-slip system $\left(\left\{10\bar{1}4\right\}\ \langle\bar{2}021\rangle\right)$, and glide of the *f*-slip system $\left(\left\{\bar{1}012\right\}\ \langle 2\bar{2}01\rangle\right)$ are from Turner et al. (1954) and shown for comparison with yield measurements.

show the data of Renner and Rummel (1996) for *m* at room temperature and under dry conditions (Table 4). Similar to *h*, at room temperature pore water has no measurable effect on the dilatancy coefficient, *m*, although there may be a weak effect at pressures greater than 100 MPa (Figure 5d). Like its effect on hardening, temperature seems to suppress dilatancy under dry conditions (Figure 5d).

3.2. Structural Observations

At all temperatures and water saturation conditions, cores that strain weaken exhibit localized shear fractures that cross-cut the entire core and those that strain harden exhibit macroscopically distributed deformation. This correlation between strain hardening and distributed deformation occurs even when strain hardening occurs with dilatant deformation. At the lowest effective pressures and temperatures, transgranular fractures consist of several anastomozing strands (Figure 7a). The orientations and number of transgranular shear fractures were measured from thin section scans. If a transgranular fracture changes orientation by more than 10°, it was measured as

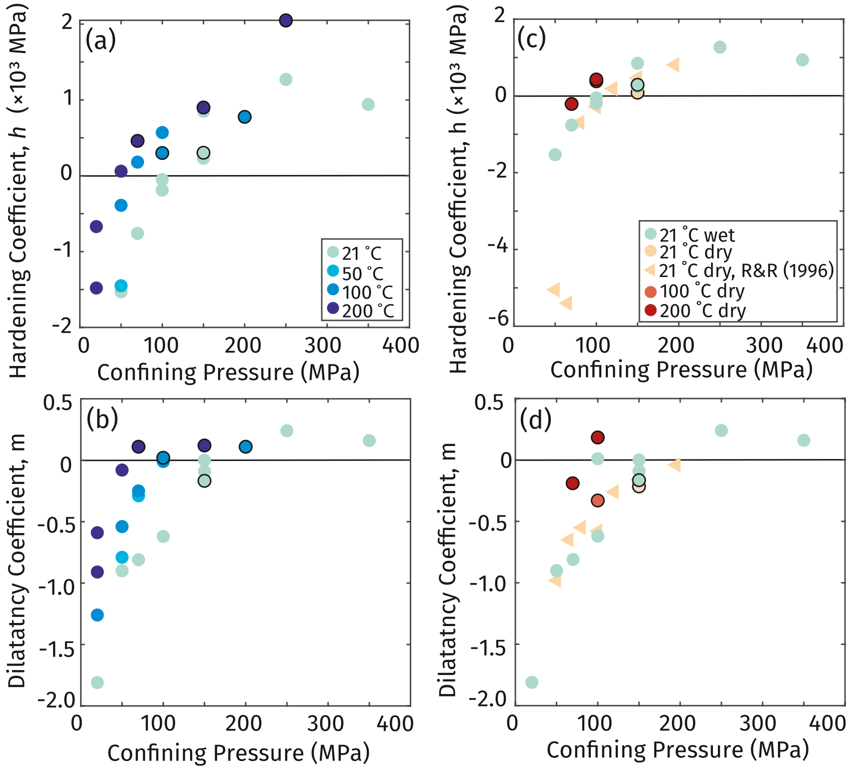

Figure 5. The hardening coefficient, *h* (a) and dilatancy coefficient, *m* (b) for water-saturated samples as a function of effective confining pressure at different temperatures. The hardening coefficient, *h* (c) and dilatancy coefficient, *m* (d) for dry samples as a function of effective confining pressure at different temperatures. Our results for water-saturated limestone at room temperature are shown for comparison. The hardening coefficient is defined as $h = \partial\sigma_d/\partial\epsilon_a$, where positive *h* indicates strain hardening, and the dilatancy coefficient is defined as $m = \partial\epsilon_V/\partial\epsilon_a$, where positive *m* indicates compaction. The data for dry samples are from both our experiments and the results of Renner and Rummel (1996 R & R, 1996). Data from our experiments conducted with the Paterson apparatus are outlined in black and those conducted with the Goetze apparatus are without outlines.

a separate fracture. We have the most observations of localized deformation at room temperature and 100°C (Figure 8). At room temperature, the average angle between fracture plane and core axis increases with pressure from 14° to 30° at room temperature, and remains relatively constant at ~40° at 100°C. With increasing pressure and temperature, the shear fractures become more planar and the orientations of fractures become less variable, reflected in the lower standard deviation at these conditions. In samples that experienced distributed deformation,

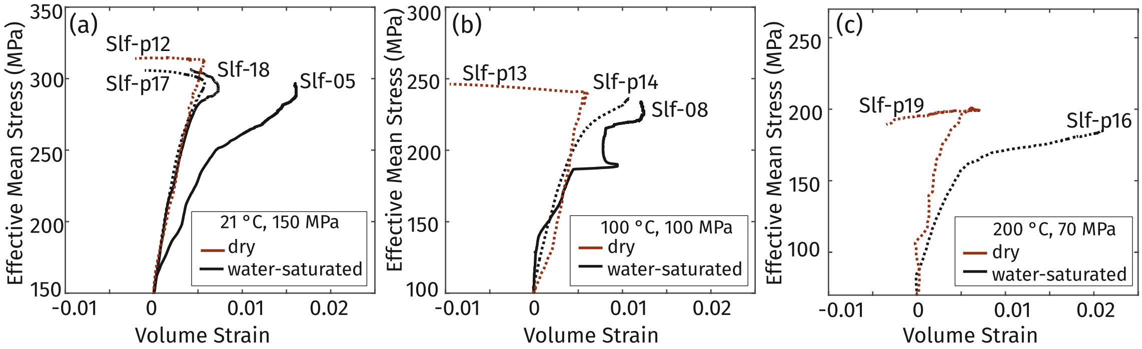

Figure 6. Comparison of the effective mean stress ($\sigma_d/3 + \sigma_3 - P_f$) vs. volumetric strain of experiments conducted dry and water-saturated at the same effective confining pressure and temperature. Volumetric strain is set to zero at the start of triaxial loading. (a) Room-temperature (21°C) and 150 MPa effective confining pressure, (b) 100°C and 100 MPa effective confining pressure, and (c) 200°C and 70 MPa effective confining pressure. Data for samples deformed in the Goetze apparatus are shown with solid lines and those deformed with the Paterson apparatus are shown in dashed lines.

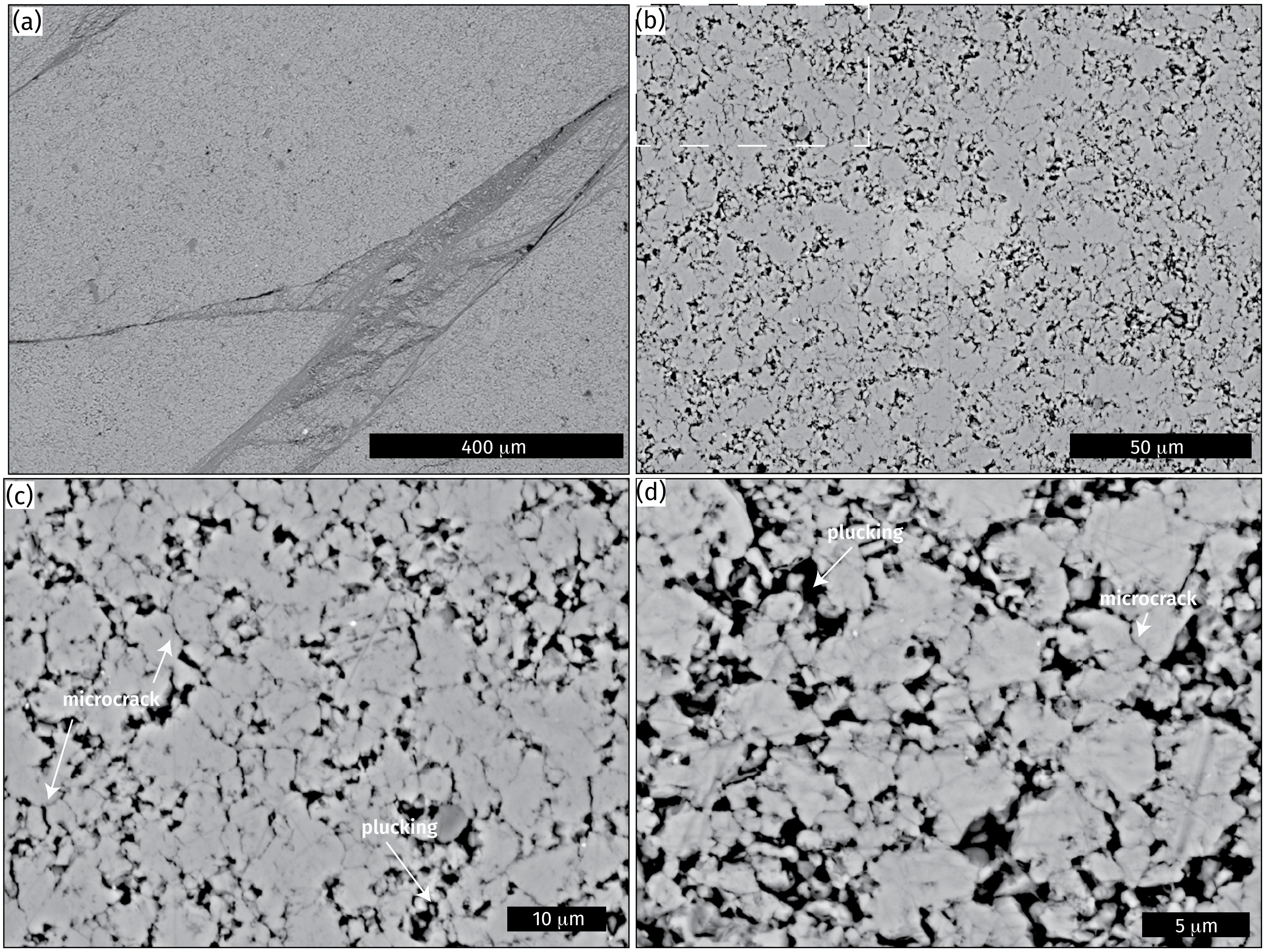

Figure 7. Back scattered electron (BSE) images showing microstructures that develop in water-saturated Solnhofen limestone samples. (a) Transgranular shear fractures that developed at room temperature and 50 MPa effective pressure (Slf-01; Table 1). (b) Distributed deformation in a sample deformed at 100°C and 70 MPa effective pressure (Slf-15). (c) Higher magnification image of the dashed box region in (b). (d) High magnification image of a sample deformed at 100°C and 100 MPa effective pressure (Slf-08). In all images σ_1 is vertical.

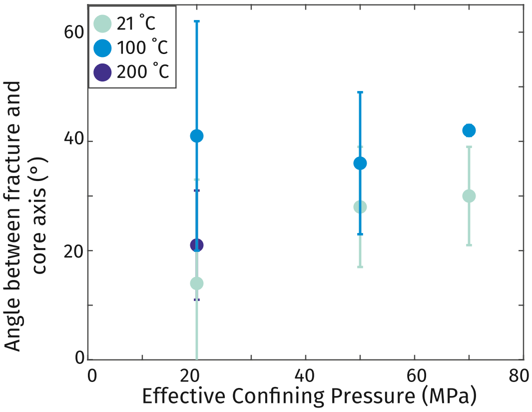

Figure 8. The angles between the planes of transgranular shear fractures and the core axis for water-saturated Solnhofen limestone at different pressures and temperatures. The average angle for each sample is shown and bars indicate the standard deviation.

the limestone structure appears homogeneous at the hand sample scale and there is no evidence of transgranular fracturing (Figure 7b).

Within localized transgranular shear fractures, calcite grains show evidence of microfracturing and twinning (Figures 7a and 9a). Twinning is indicated by abrupt tabular differences in surface morphology in SE images that follow the expected geometry for twins, and we interpret that differences in crystallographic orientation of twins resulted in slight differences in polishing that stand out in SE images (Figure 9). Intergranular fractures occur along grain boundaries and some intragranular microfractures occur in a morphology the resembles cleavage or twinning in calcite (Figure 7b; Demurtas et al., 2019). Samples that exhibit distributed deformation show evidence of grain boundary microfracturing and some intragranular microfracturing (Figures 7c and 7d). These samples were also more prone to plucking during this section preparation which may have preferentially removed fracture grains.

The EBSD measurements support the occurrence of low-temperature crystal plasticity (twinning and dislocation glide) in calcite (Figure 10). The

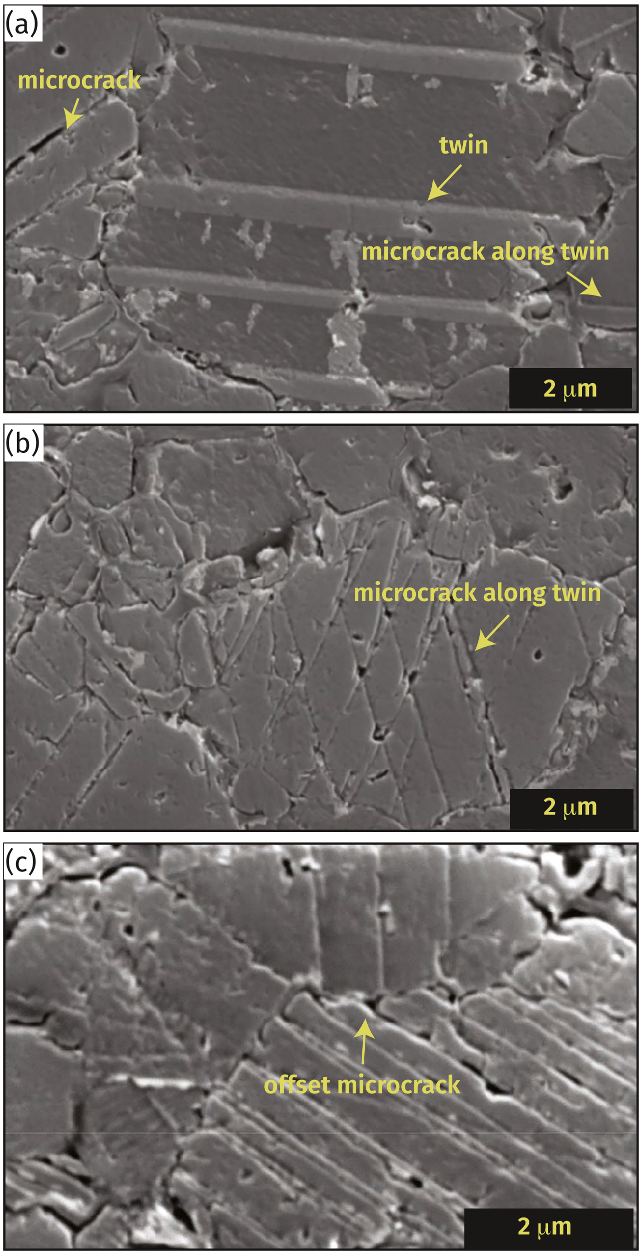

Figure 9. Secondary electron images showing evidence of microfracture and twin relationships under brittle deformation conditions. (a) Sample Slf-02 (Table 1), deformed water-saturated at room temperature (21°C) and 100 MPa effective pressure near the brittle to ductile transition. Deformation was slightly strain weakening, localized, and dilatant. Twins are evident as changes in the sample topography. Microcracks have sharp linear traces and are closely spaced. In some cases microcracks clearly form along twins. (b) Sample Slf-02. An example of fracture sets that form angles consistent with angles between e-twins. (c) Sample Slf-14 deformed water-saturated at 200°C and 20 MPa effective pressure. Deformation was strain weakening, localized, and dilatant. Examples of microcracking along inferred twin planes are observed, and some microcracks show evidence of shear offset.

misorientation angle is a measure of the difference in crystallographic orientation between two grains; the formation of subgrains through dislocation glide can be inferred when misorientation angles less than 10°–15° occur between neighboring pairs of calcite grains with a greater incidence than misorientation angles between random pairs of calcite grains. In our data, calcite grains show a peak at less than 5°, which indicates that new subgrains formed through dislocation glide (Figure 10b; e.g., Valcke et al., 2006). Another peak occurs near 78°, which is a characteristic angle for twins that formed along *e*-planes $\left(\left\{01\bar{1}8\right\}\right)$ in calcite and indicates the operation of twinning during deformation.

3.3. The Brittle to Ductile Transition

We summarize the effects of pore water and temperature on the brittle to ductile transition from our results on water-saturated Solnhofen limestone at 21°C, 100°C, and 200°C and previous studies that have documented this transition. Our observations and those of Renner and Rummel (1996) show that strain weakening mechanical behavior consistently correlates with localized deformation under all fluid conditions and temperatures in the Solnhofen limestone, whereas strain hardening behavior correlates with macroscopic distributed deformation regardless of more complex volumetric strain patterns, which is a correlation well-documented in rock mechanics. Accordingly, we characterize the effective pressure of this transition as the brittle to ductile transition (Rutter, 1986). Strain hardening and distributed deformation of our Solnhofen samples may eventually lead to strain weakening and localized deformation with sufficient strain. Under water-saturated conditions, the pressure of this transition in the Solnhofen limestone is determined from our data and that of Heard (1960) and Rutter (1972) between room temperature and 300°C. Under dry conditions, the transition is documented at temperatures between room temperature and 400°C by Baud, Zhu, et al. (2000), Heard (1960), Renner and Rummel (1996), and Rutter (1972). This compilation shows that at room temperature the transition occurs at a similar effective pressure (100 MPa) regardless of pore water content (Figure 11). The effective pressure of the brittle to ductile transition decreases approximately linearly with increasing temperature under both dry and saturated conditions; however, under water-saturated conditions the effective pressure of this transition is reduced more with increasing temperature.

4. Discussion

We documented correlations between strength and pressure, temperature, and water content across the brittle to ductile transition of the Solnhofen limestone. Overall, we find that water and temperature both weaken the Solnhofen limestone, but in different ways. At room temperature and pressures less than 200 MPa, water weakens the yield strength and the strength at 4% axial strain, but has no measurable effect on the peak strength or the pressure of the brittle to ductile transition (Figures 4 and 11). Under water-saturated conditions, temperature has no clear effect on the yield strength, but weakens both the peak strength and strength at 4% axial strain, and reduces the pressure of the brittle to ductile transition. To understand this complex behavior, we evaluate the roles of pore water and temperature on low-temperature (≤200°C) deformation mechanisms in calcite and the resulting mechanical behavior of limestone.

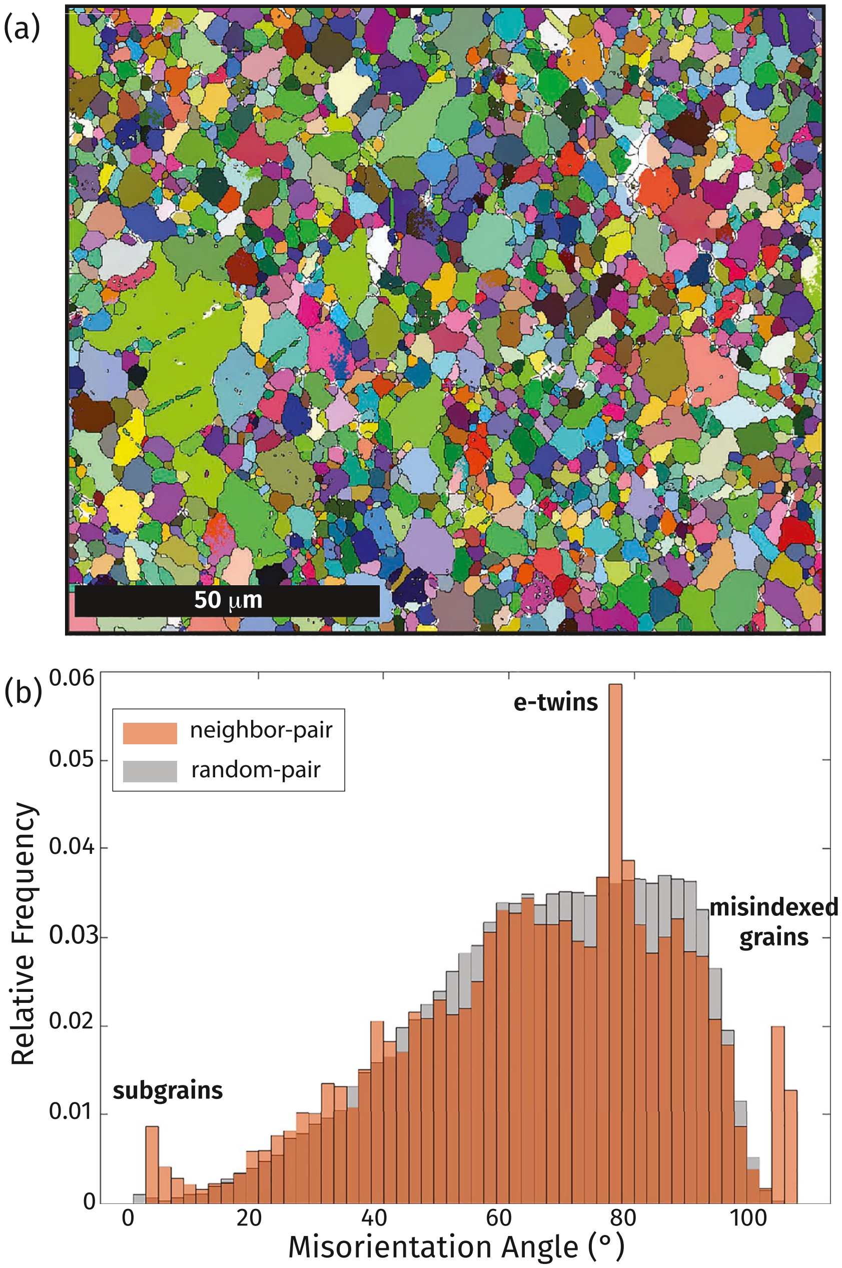

Figure 10. EBSD data for sample Slf-02 (Table 1), deformed water-saturated at room temperature (21°C) and 100 MPa effective pressure near the brittle to ductile transition. (a) Orientation map color coded according to the Euler angles with a grid spacing of 0.2 μm. (b) Misorientation angles were determined between random pairs of calcite grains (gray) and neighboring pairs of calcite grains (orange). Histograms of misorientation angles are binned every 2°. The peaks at <5° and near 78° correspond to subgrain formation and e-twinning, respectively. A discussion of the peak at 103° due to misindexing is found in Bestmann and Prior (2003). Data were processed and plotted using the MTex Matlab toolbox (Mainprice et al., 2011).

4.1. Micromechanics of Limestone Deformation

Limestone deforms by brittle faulting under low effective pressures. Microcrack nucleation and coalescence into macroscopic shear fractures is generally attributed to wing crack growth using the model of Ashby and Sammis (1990). For the Solnhofen limestone deformed under dry conditions and at room temperature Baud, Zhu, et al. (2000) showed that during the initial deformation after yield, the collapse of spherical pores facilitates shear-enhanced compaction, strain hardening, and distributed deformation. At high enough strains, plastic

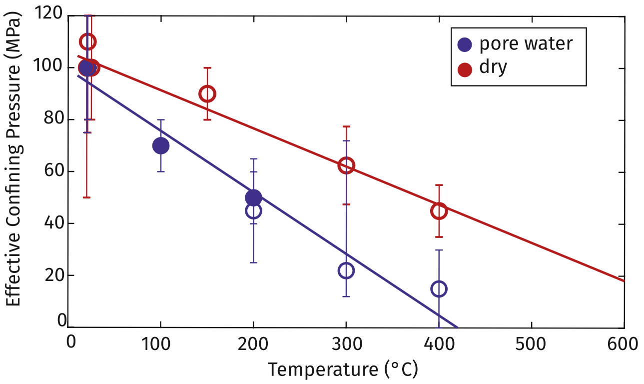

Figure 11. The confining pressure at the transition from brittle to ductile deformation as a function of temperature both dry and with pore water. The transition is defined here by the pressure at which strain weakening and macroscopic localized deformation cease to occur. Data are compiled from this study (filled circles, saturated) and previous studies (hollow circles). Heard (1960): dry (4 points); Rutter (1972): saturated (3 points) and dry (1 point); Renner and Rummel (1996): dry (2 points); Baud, Zhu, et al. (2000): dry (1 points). Because the brittle to ductile transition occurs as a change in behavior with increasing effective pressure, an exact transition pressure is an estimate; uncertainty is an average of one half the difference in effective pressure of experiments used to identify the transition. The linear fits are shown along with error bars indicated with shading.

pore collapse and compaction eventually give way to dilatant cracking, although deformation may remain strain hardening and distributed. Baud, Zhu, et al. (2000) proposed that these cracks were nucleated by dislocation pile-ups. Nicolas et al. (2017) developed more detailed micromechanical models that called upon a combination of these deformation mechanisms to successfully describe the mechanical properties of the Solnhofen limestone and more porous limestones under dry conditions and at room temperature. Because of the success of these models under dry conditions, we evaluate the anticipated effects of pore water and temperature on these processes to guide the interpretations of our observations.

4.1.1. Brittle Deformation

Brittle deformation occurs by the formation and coalescence of dilatant microcracks, and the wing crack model is particularly useful for understanding fracturing of low-porosity rocks (Ashby & Sammis, 1990). Wing cracks initiate when the maximum principal stress reaches a critical stress, σ_{1C}, that is a function of the friction coefficient between calcite grains, μ, the critical stress intensity factor for calcite, K_{IC}, and the initial flaw size, $2a$.

$$\sigma_{1C} = \frac{\sqrt{1+\mu^2}+\mu}{\sqrt{1+\mu^2}-\mu}\sigma_3 + \frac{\sqrt{3}}{\sqrt{1+\mu^2}-\mu}\frac{K_{IC}}{\sqrt{\pi a}} \tag{1}$$

The growth and coalescence of wing cracks then gives rise to shear fracture formation and strain weakening with the peak strength approximated by Ashby and Sammis (1990) and Baud, Zhu, et al. (2000). In this model damage is quantified by the parameter A, which evolves from an initial value, $A_0 = \pi(a\cos\gamma)^2 N_A$ according to $A = \pi(l + a\cos\gamma)^2 N_A$, where N_A is the number of cracks per unit area having an orientation $\gamma = 0.5\tan^{-1}(1/\mu)$ and l is wing crack length. As a result of progressively increasing wing crack length, σ_1 evolves with A according to:

$$\sigma_1 = \left[C_1 + \frac{C_4\left(\sqrt{A/A_0}-1\right.}{a+\sqrt{\pi A_0}\frac{\sqrt{A/A_0}-1}{1-\sqrt{A}}}\right]\sigma_3 + \frac{\left(\sqrt{A/A_0}-1+0.1/\cos\gamma\right)(1/2)}{1+\sqrt{\pi A_0}\frac{\sqrt{A/A_0}-1}{1-\sqrt{A}}}\frac{C_4}{\sqrt{\cos\gamma}}\frac{K_{IC}}{\sqrt{\pi a}} \tag{2a}$$

$$C_1 = \frac{\sqrt{1+\mu^2}+\mu}{\sqrt{1+\mu^2}-\mu} \tag{2b}$$

$$C_4 = \sqrt{30}\cos\gamma/\left(\sqrt{1+\mu^2}-\mu\right) \tag{2c}$$

Because the differential stress at which wing cracks grow increases with σ_3 (Equation 1), when mechanical yield represents the growth of cracks it should also increase with pressure. The pressure independence of yield suggests that either microcracking and pore collapse do not contribute to deformation at very small strains (Figures 4a and 4c). Instead, this observation is consistent with the hypothesis that yield occurs at the onset of low-temperature crystal plasticity (dislocation glide and twinning), which are pressure-independent mechanisms. The differential stresses at yield are significantly higher than the critical resolved shear stress required for twinning on the e-planes defined by twinning on the $\left\{01\bar{1}8\right\}$ planes and are sufficient to activate dislocation glide of the r-slip system defined by the families of planes $\left\{10\bar{1}4\right\}$ and directions $\langle\bar{2}021\rangle$ (Figures 4a and 4c). That pressure-insensitive yield eventually evolves to dilatant (pressure-sensitive) fractures indicates that fracturing contributes more to the overall strain than crystal-plastic processes. The onset of wing crack growth, σ_{1C}, must therefore occur at stresses greater than the plastic yield stress. Our results combined with Fredrich et al. (1989) indicate that yield strength may be lower under water-saturated conditions, which is not consistent with the expected insensitivity of crystal plasticity to water. If these results are correct it may be that twins and dislocations act as sites of fracture nucleation; under water-saturated conditions microfracturing may then be enhanced and result in a more obvious deviation of the stress-strain curve from linear at lower stresses. The interaction of fracture and crystal plasticity is supported by microscopy and EBSD data of Slf-02 showing evidence of fracturing along twins planes (Figures 9 and 10) and by experiments on Carrara marble (Rybacki et al., 2021).

The peak strength at which the wing cracks coalesce (Section 4.1.1) increases with increasing μ and K_{IC}. Pore water typically reduces the critical fracture toughness, K_{IC}, through a decrease in the surface energy (Atkinson, 1984), and is shown to reduce surface energy and K_{IC} in both single crystals of calcite and marble samples by up to 50% at room temperature (Røyne et al., 2011; Voigtländer et al., 2018). Although less data are available at elevated temperature, Chandler et al. (2017) saw no measurable effect of temperature on K_{IC} in dry calcite. The effect of temperature under water-saturated conditions is unknown, but (Jefferd et al., 2021) a 2%–3% reduction in K_{IC} in sandstone between 20°C and 150°C, which explained water weakening of the peak strength. Thus the effect may be small but non-negligible in calcite as well. We are not aware of data for the effect of water on the coefficient of friction, μ, between calcite mineral surfaces. The bulk dynamic friction coefficient of calcite gouge depends on both fluid conditions and temperature, and we take this as the best approximation of these effects while acknowledging that measurements of gouge friction also likely reflect cataclasis. At room temperature, water reduces dynamic μ of dry pure calcite gouge by 8% and the effects of temperature depend on the fluid conditions (Verberne et al., 2014). Whereas the frictional strength of dry calcite gouge increases approximately 5% between room temperature and 150°C, when pore water is present frictional strength decreases 26% between room temperature and 200°C (Verberne et al., 2014, 2015).

Thus, when the effects of pore water on K_{IC} and μ are considered, the wing crack model predicts a reduction of the peak strength under water-saturated conditions relative to dry conditions. Additional weakening is expected with increasing temperature under water-saturated conditions, in contrast to dry conditions for which temperature is expected to have a small strengthening effect. These anticipated effects generally explain the weakening of peak strength with temperature under water-saturated conditions, although our limited data that show no measurable temperature dependence of peak strength under dry conditions (Figure 4). However, this model does not explain the fact that at room temperature the peak strengths are similar under dry and water-saturated conditions. Nicolas et al. (2016) also observed that the peak strength of Tavel limestone is unaffected by pore water at room temperature and suggested that during wing crack growth, the fracture tip remains dry. Although this explanation is plausible if only room temperature is considered, this supposition fails to explain how, if the crack tip remains dry, temperature then has a measurable effect under water-saturated conditions. Interestingly, the unconfined compressive strength of carbonates is shown to be reduced by pore water consistent with the wing crack model (Baud et al., 2016; Rabat et al., 2020). One possibility is that crack tips are not completely dry, but that pore pressure is reduced in the crack tip during our experiments leading to strengthening relative to predicted water-saturated strength. This would not occur in uniaxial compressive strength tests because the pore water is not pressurized. Similar effects of pore water have been documented in crystalline silicate rocks (Hadizadeh & Law, 1991; Wang et al., 2013), but sandstones more consistently exhibit water weakening of the peak strength (Baud, Schubnel, & Wong, 2000; Hadizadeh & Law, 1991; Noël, Baud, & Violay, 2021). The water-weakening behavior of silicate rocks may be explained by the anticipated differences in the permeability and fracture geometry of these rocks supporting the hypothesis that crack tips either remain dry or have reduced pore pressure over the time scale of fracture propagation.

In addition to chemical effects of water on fracturing, pore water can influence deformation through the process of dilatant hardening which occurs when pore and fracture volume increases and the pore pressure correspondingly decreases under undrained deformation conditions (Brace & Martin, 1968; Schmitt & Zoback, 1992). Although our calculations showed that the experimental system is drained during deformation (Section 2.3), dilatant hardening can be important locally around disconnected pores or during fracture coalescence when deformation rates are locally higher than the imposed strain rates (e.g., French & Zhu, 2017; Ougier-Simonin & Zhu, 2013). Despite the fact that our pore fluid pressures were relatively high (50 MPa) so that the effect of dilatant hardening on strength could be significant, we did not measure peak strengths that were unrealistically high under saturated conditions, such as higher than the peak strength under dry conditions at the same effective pressure (Brace & Martin, 1968). This is consistent with drained deformation conditions. However, it is possible that dilatant hardening contributes to the fact that the peak strength is similar under water-saturated and dry conditions even though micromechanical models predict water weakening.

4.1.2. Ductile Deformation

After the initial yielding, the strength of Solnhofen at a given strain is reduced either by adding pore water or by increasing the temperature (Figures 3, 4 and 6). In the conceptual model of Baud, Zhu, et al. (2000), ductile deformation initiates when effective pressures suppress dilatant microcracking and promote the compaction of spherical pores by water-insensitive dislocation glide normal to pore boundaries. At high strains during ductile deformation microcracking might eventually occur at pore boundaries as dislocations become tangled; this microcracking would, of course manifest as dilatant deformation. The observation that the presence of water increases compaction and decreases dilatancy is, however, inconsistent with the notion that glide processes are insensitive to the presence of water or that microfracturing is enhanced by fluids. We interpret that at least some of this compaction and weakening occurs by grain boundary and more limited intragranular microfracturing based on our microstructural observations. In addition, it is possible that compaction is promoted by dissolution processes within the pores.

Dissolution and precipitation of calcite are activated by water at the relatively low temperatures of our experiments, and dissolution of calcite is shown to have significant effects on rock strength Lisabeth and Zhu (2015). Although the pore fluids were allowed to equilibrate with the rock for 48–96 hr at ambient conditions prior to testing to minimize this effect, small amounts of dissolution or precipitation may have occurred due to increases in pressure and temperature during the experiments (Segnit et al., 1962). Unlike most other minerals, the solubility of calcite decreases with increasing temperature (Segnit et al., 1962), and we, therefore, expect any deformation and weakening due to dissolution to decrease with increasing temperature. At effective pressures less than 200 MPa, σ_F in water-saturated limestone decreases with increasing temperature, inconsistent with behavior expected if dissolution is the only control on pore collapse (Figure 4b). Accordingly, continued thermally activated microfracturing and low-temperature plasticity is still required in parallel with dissolution to explain the temperature effect. At effective pressures greater than 200 MPa, we see an apparent evolution to temperature-strengthening behavior. Although not the focus of this study, this behavior is consistent with expected patterns if compaction is facilitated primarily by dissolution, may be due to a reduction in fracturing with increasing pressures, and warrants more focused study.

Furthermore, pressure solution creep has been documented at relatively low temperature in calcite-rich rocks, previous experiments have shown that pressure solution creep of limestone occurs experimental strain rates on the order of 10^{-8} s^{-1}, which is three orders of magnitude lower than strain rates in our experiments (Brantut et al., 2014). There are a number of pressure solution flow laws whose form depend on porosity and grain packing. To evaluate the plausibility that pressure solution creep was active in these experiments, we employ the flow law for diffusion-limited creep through a thin film (den Brok, 1998; Rutter & Elliott, 1976).

The strain rate due to diffusion limited pressure solution creep is:

$$\dot{\epsilon} = \frac{A_R \Omega \rho_f c\,(T, \rho_w)\, D(T) w \sigma_d}{\rho_s RT d^3} \tag{3}$$

where $A_R = 44$ is a geometric constant for spherical grains, $\Omega = 3.7 \times 10^{-5}$ m^3/mol is the molar volume of calcite, ρ_w is the fluid density as a function of fluid pressure and temperature (Burnham et al., 1969), ρ_s is the solid density (2,710 kg/m^3), $w = 1$ nm is the thin film width (Renard et al., 1997), R is the gas constant, $d = 10$ μm is the grain size, and T is the temperature in K. The solubility of calcite, $c(T, \rho_w)$, is in mole fraction and is a function of temperature and fluid density. We use the result of Caciagli and Manning (2003) that the molal solubility, α is given by $\log\, \alpha = -3.95 + 0.00266T + (32.8 - 0.0280T)\log\, \rho_w$. The diffusivity, $D(T)$, is a function of temperature and is given by $D(T) = 4.3 \times 10^{-8} \exp(-(15 \text{ kJ/mol})/(RT)$; Nakashima, 1995; Zhang et al., 2010).

We use Equation 3 to calculate the strain rate due to pressure solution creep at our experimental temperatures and measured differential stresses (σ_d). We find that at room temperature and the highest differential stresses measured (450 MPa), the anticipated pressure solution creep strain rate is ~2×10^{-7} s^{-1}. With increasing temperature, this strain rate increases slightly to ~3×10^{-7} s^{-1} at 100°C and ~3.5×10^{-7} s^{-1} at 200°C. These calculated strain rates are two orders of magnitude slower than our experimental strain rates, indicating that we cannot clearly attribute deformation to pressure solution in these experiments. We note that constitutive relations for pressure solution of granular materials take into account stress concentrations at grain contacts and tend to predict higher pressure solution creep rates (e.g., Zhang et al., 2010). However, these models have not been validated for carbonates of low, but non-negligible porosity (1%–5%), and better constraints are clearly needed.

4.2. Controls on the Brittle to Ductile Transition

Our ability to document the dependence of the brittle to ductile transition on pore water and temperature is due in part to the large number of experimental studies on the Solnhofen limestone. The transition from strain weakening to strain hardening with increasing pressure and the associated transition from localized to distributed deformation is well-described in water-saturated and dry Solnhofen limestone (Baud, Zhu, et al., 2000; Heard, 1960; Renner & Rummel, 1996). A similar transition also occurs in more porous carbonates (Lisabeth & Zhu, 2015; Nicolas et al., 2016; Renner & Rummel, 1996; Vajdova et al., 2004) and clastic silicates (Brace, 1978; Edmond & Paterson, 1972; Wong et al., 1997), and less porous marbles (Fredrich et al., 1989). Unfortunately, the dependence of this transition on temperature and pore fluids, and links to the underlying mechanisms, are poorly described in all lithologies although existing data show a tendency for the pressure of this transition to decrease with water or temperature. Nicolas et al. (2016) presented results consistent with ours for the more porous (15%) Tavel limestone. They showed the brittle to ductile transition occurs at lower pressures at 70°C than at 20°C under dry conditions, and the pressure of this transition is the same under water-saturated and dry conditions at 20°C, indicating that similar processes may control the brittle to ductile transition in more porous limestone as well. In siliclastics, Jefferd et al. (2021) showed that the pressure of the brittle to ductile transition decreases from 20°C to 150°C in water-saturated sandstone which they attributed to enhanced cataclastic pore collapse, a conclusion consistent with the observation that cataclasis is prevalent in siliclastic rocks at low temperatures. This is similar to our conclusion in the Solnhofen limestone but more expected as cataclastic pore collapse operates under dry conditions in sandstones as well (Wong et al., 1997).

Our observation that the strain hardening and dilatancy coefficients, h and m, are independent of water content at room temperature is consistent with the fact that the brittle to ductile transition is also independent of water content at room temperature (e.g., Rudnicki & Rice, 1975). That water enhances h and m at elevated temperature (Figures 5a and 5b) is also consistent with the combined effects of water and temperature on the brittle to ductile transition (Figure 11). The observed dependencies of the brittle to ductile transition cannot be simply explained by the anticipated effects of water on the individual processes of wing-crack growth, plastic pore collapse, or dissolution. Because these processes operate concurrently rather than in isolation, it is possible that changes in the relative rates of the processes are important.

The processes that contribute to deformation, and therefore the brittle to ductile transition, under water-saturated conditions are enhanced microfracturing and dissolution with concomitant dislocation glide and twinning. To evaluate the effects of water and temperature on the relative rates of the various processes, we start with the micromechanics of deformation for dry Solnhofen limestone at room temperature presented by Baud, Zhu, et al. (2000) and then consider the roles of pore water. In their model, localized, strain weakening deformation occurs at low pressures by wing crack growth whereas distributed, strain hardening deformation occurs at high pressures by the collapse of pores by crystal plasticity. The transition between these modes of deformation occurs at the pressure (σ_3) at which the strength to deform by plastic pore collapse becomes lower than the stress required for wing crack nucleation (Equation 1), and we take this as the pressure for the brittle to ductile transition. Baud, Zhu, et al. (2000) fit their data to Equation 1 and report that $\mu = 0.53$ and $K_{IC}/\sqrt{\pi a} = 97$ MPa; however, we were unable to reproduce this fit. We were able to fit their data with $\mu = 0.53$ and $K_{IC}/\sqrt{\pi a} = 57$ MPa, which is also closer to the value of 67 MPa that Ashby and Sammis (1990) report to fit the Solnhofen data of Heard (1960). For dry conditions, we approximate that K_{IC} as temperature-independent, and we use the results of Verberne et al. (2014) to approximate the temperature-strengthening effect on μ as 0.04%/°C. We also include the temperature-dependent shear and bulk moduli from Dandekar (1968) in the plastic pore collapse model.

To determine the yield stress for plastic pore collapse, Baud, Zhu, et al. (2000) used the model of Curran and Carroll (1979). In this model, shear stress concentrations at the boundaries of spherical pores are locally high enough to reach the yield strength for low-temperature plasticity, Y, which causes shear-enhanced collapse of the pore space. Baud, Zhu, et al. (2000) inferred that pore collapse occurs primarily through dislocation glide, but there is no reason that Y does not also reflect contributions from twinning in well-oriented grains. Complete details of this model are provided in Equations A1 through A4F in the Appendix of Baud, Zhu, et al. (2000), which corrects typographical errors in the original manuscript of Curran and Carroll (1979), but the general form is based on the von Mises yield criterion where $\sqrt{J} = Y/\sqrt{3}$ and J is the second invariant of the deviatoric stress. In this model, the yield envelope depends on the elastic moduli of calcite and the porosity, ϕ of spherical pores in addition to Y. We employ the porosity of spherical pores determined by (Baud, Zhu, et al., 2000; $\phi = 0.028$) and the room temperature plastic yield value they determined from fitting the data ($Y = 975$ MPa).

To evaluate the role of temperature on yield stress, we scale the room temperature value of $Y = 975$ MPa to temperatures up to 400°C using the flow law determined by (Sly et al., 2019) from micro-indentation tests. Those authors processed their data following Ginder et al. (2018) and fit the results to a low-temperature creep law owing to Frost and Ashby (1982). The Frost and Ashby (1982) flow law does not include strain hardening, but it may work well for determining the yield point. Strain rate, $\dot{\epsilon}$ is given by:

$$\dot{\epsilon} = 2 \times 10^{10} \sigma_Y^2 \exp\left(\frac{-H}{RT}\left(1 - \frac{\sigma_Y}{\sigma_{PN}}\right)\right) \tag{4}$$

where H is activation enthalpy (200 kJ/mol), R is the gas constant, $\sigma_{PN} = 1.21$ GPa is the Peierls stress, and σ_Y is differential yield stress in GPa.

At room temperature, these micromechanical models predict a brittle to ductile transition at 100 MPa, consistent with several experimental studies (Figure 12a). Furthermore, the temperature dependencies of wing crack nucleation and plastic pore collapse are consistent with the temperature dependence of the brittle to ductile transition under dry conditions. This temperature effect is primarily due to thermal weakening of the yield strength for plastic pore collapse, but the small increase in wing crack nucleation strength with increasing temperature contributes to this effect (Figure 11a).

To assess the effects of water on the brittle to ductile transition, we evaluate the wing crack model using the known weakening effects of water on K_{IC} and μ. We assume K_{IC} is reduced 50% due to the presence of water (Røyne et al., 2011; Voigtländer et al., 2018), but is independent of temperature (e.g., Zhao et al., 2020). We also assume that μ is reduced 8% by pore water and an additional 26% between room temperature and 200°C based on the data of Verberne et al. (2014, 2015). Although Nicolas et al. (2016) inferred a 6% reduction in K_{IC} and 50% reduction in μ with the addition of pore water by inverting the wing crack model using experimental data, we adjust these variables using the results of more targeted experiments.

To estimate how much temperature weakens the Solnhofen during pore collapse, we reverse the process used to evaluate the brittle to ductile transition under dry conditions. We assume the pressure of the brittle to ductile transition follows the water-saturated result shown in Figures 11 and 12b. We then evaluate what the “effective yield strength” of the calcite must be to result in the observed brittle to ductile transition. Although the pore collapse model is developed for crystal plastic yield at the pore wall, empirical elliptical cap models are commonly employed to characterize shear-enhanced compaction (e.g., Wong et al., 1997). Thus, our estimated yield strength is an “effective yield strength” that encompasses the inferred weakening to due glide, twinning, microfracturing, and dissolution. We find that to explain the observed effects of water and temperature on the brittle to ductile transition, the effective yield strength of calcite in the plastic pore collapse model must decrease 32% relative to dry conditions at room temperature up to 61% relative to dry conditions at 300°C (Figure 12c).

5. Geologic Implications

Understanding the combined role of temperature and pore water on the deformation of limestone is critical to appropriate rheologic modeling of many tectonic systems, including subduction plate boundaries. At the highest effective pressures that we studied (>200 MPa), the mechanical behavior shows evidence of weakening that may reflect additional deformation processes that include enhanced crystal plasticity or dissolution precipitation mechanisms. Thus, our inference about ductile deformation mechanisms and the brittle to ductile are relevant to the effective pressures investigated. Our results provide several key observations for constraining deformation of carbonate systems in the Earth. More porous limestones show that pore collapse, compaction, and strengthening occur at relatively low pressures and temperatures (Brantut et al., 2014; Lisabeth & Zhu, 2015). As a result, the low porosity Solnhofen limestone may have structural features and strength that are pertinent to rocks at depth.

During subduction, the conditions that promote brittle or ductile deformation may be complex owing to the dependence of this transition on not only temperature, but also porosity, pore fluid chemistry, strain rate, and the

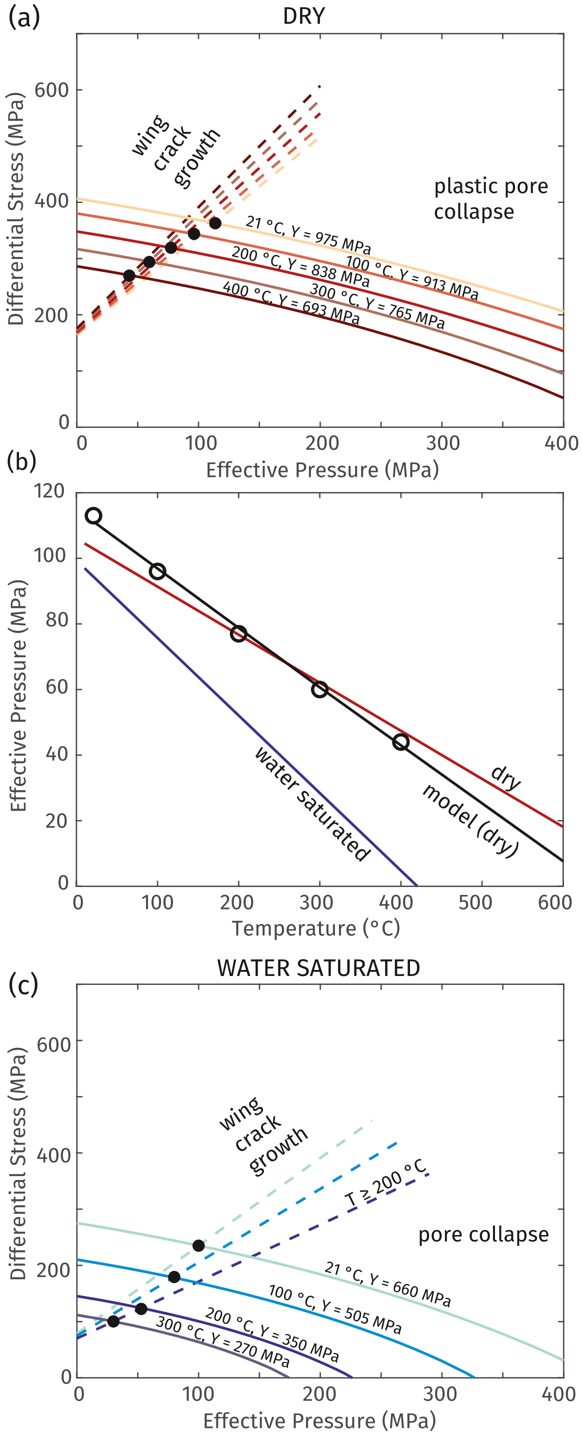

Figure 12. (a) The predicted strength for plastic pore collapse is shown for different temperatures with solid lines and the predicted strength for wing crack growth as a function of effective confining pressure is shown with dashed lines. The colors of solid and dashed lines correspond to temperature. Where the two intersect approximates the effective pressure of the brittle to ductile transition. The models are both assuming dry conditions. (b) The predicted effective pressure of the brittle to ductile transition using the models in (a) as a function of temperature (black line) and best fits to the compiled experimental data showing the effects of temperature on the brittle to ductile transition for dry conditions (red) and water-saturated conditions (blue). (c) The predicted strength from wing crack growth shown with dashed lines assumes properties of water-saturated rock. The plastic pore collapse models at different yield stresses, which were fit to result in brittle to ductile transitions for water-saturated Solnhofen limestone in (b) at the indicated temperatures.

details of the loading geometry (Zhu et al., 2010). For instance, subducted porous sediments are likely to deform in the ductile field by cataclastic pore collapse at very shallow conditions (<1 km; Baud et al., 2009; Lisabeth & Zhu, 2015). The resulting strengthening due to porosity reduction may then promote brittle deformation. However, our results indicate that even at relatively low porosities, ductile deformation may occur at relatively shallow conditions when the effects of pore fluid and temperature are considered. Strain rates lower than experimental rates are likely to reduce the pressure of this transition even more through a reduction in the strength of plastic pore collapse provided, of course, that the pore space is drained. As an example, comparing experimental constraints on the brittle to ductile transition to geothermal constraints on the northern Hikurangi margin (Antriasian et al., 2019), our results indicate that even for a very low porosity carbonate, a final transition to ductile deformation is expected by 8–10 km depth and within a region of shallow slow slip. Thus, understanding the slow slip process may rely on the constitutive behavior and mode of deformation in limestone.

Previous studies on the deformation of more porous limestones show reductions in strength with increasing temperature and the presence of pore fluids that are qualitatively consistent with those of our experiments (Brantut et al., 2014; Lisabeth & Zhu, 2015; Nicolas et al., 2016). These studies also interpret deformation to be through a combination of water-enhanced microcracking and low-temperature plasticity. We hypothesize that low-temperature plasticity accommodates more deformation and controls more of the mechanical behavior during deformation of the Solnhofen limestone compared to higher porosity limestones. This hypothesis is based on the observations that some aspects of the mechanical behavior of the Solnhofen seem to directly reflect low-temperature plasticity, such as pressure-independent yield strengths (Figures 4a and 4c). In addition, the near-linear evolution of strength and volumetric strain with axial strain is similar to the behavior of marbles, which is thought to reflect low-temperature plasticity (Fredrich et al., 1989). Furthermore, the strength of the Solnhofen is higher than that of higher porosity limestones, allowing sufficiently high stress for twinning and glide.

6. Conclusions

We conducted conventional triaxial compression experiments on the Solnhofen limestone to quantify the combined roles of pore water and temperature on the brittle to ductile transition in a low-porosity limestone. Experiments were conducted on samples that were either water-saturated or nominally dry, at temperatures from 21°C (room temperature) to 200°C, and at effective confining pressures from 20 to 350 MPa. We found that at the pressure, temperature, and fluid conditions tested different measures of strength cannot be easily attributed to the dominance of a single mechanism. Rather, the co-occurrence of microfracturing, low-temperature plasticity, and perhaps dissolution processes results in complex mechanical behavior. Overall, we found that, at room temperature water had no measurable effect on peak strength, strain hardening, compaction, or the brittle to ductile transition. However, under water-saturated conditions, elevated temperatures weakened the peak strength, promoted strain hardening and compaction, and reduced the pressure of the brittle to ductile transition more than under dry conditions. In particular, water and thermal weakening results in a dramatic decrease of the pressure of the brittle to ductile transition, which we attribute to enhanced microcracking. At the highest effective pressures tested, we also documented a transition to temperature strengthening behavior. This behavior might indicate the onset of dissolution mediated processes, but this hypothesis is speculative, and further study is definitely warranted.

Data Availability Statement

The experimental data are available on the Rice Digital Scholarship archive at https://doi.org/10.25611/0EMQ-H903.

Acknowledgments
MF was partially supported by NSF EAR-1452339 and WZ was partially supported by NSF EAR-1761912 and by USGS G21AP10012. The authors thank two anonymous reviewers and the editor for comments that significantly improved the manuscript.

References

Antriasian, A., Harris, R. N., Tréhu, A. M., Henrys, S. A., Phrampus, B. J., Lauer, R., et al. (2019). Thermal regime of the northern Hikurangi margin, New Zealand. *Geophysical Journal International*, *216*(2), 1177–1190. https://doi.org/10.1093/gji/ggy450

Ashby, M. F., & Sammis, C. G. (1990). The damage mechanics of brittle solids in compression. *Pure and Applied Geophysics*, *133*(3), 489–521. https://doi.org/10.1007/BF00878002

Atkinson, B. K. (1984). Subcritical crack growth in geological materials. *Journal of Geophysical Research: Solid Earth*, *89*(B6), 4077–4114. https://doi.org/10.1029/jb089ib06p04077

Bakker, R. R., Violay, M. E., Benson, P. M., & Vinciguerra, S. C. (2015). Ductile flow in sub-volcanic carbonate basement as the main control for edifice stability: New experimental insights. *Earth and Planetary Science Letters*, *430*, 533–541. https://doi.org/10.1016/j.epsl.2015.08.017

Barnes, P. M., Lamarche, G., Bialas, J., Henrys, S., Pecher, I., Netzeband, G. L., & Crutchley, G. (2010). Tectonic and geological framework for gas hydrates and cold seeps on the Hikurangi subduction margin, New Zealand. *Marine Geology*, *272*(1), 26–48. https://doi.org/10.1016/j.margeo.2009.03.012

Barthel, K. W. (1970). On the deposition of the Solnhofen lithographic limestone (lower Tithonian, Bavaria, Germany). *Neues Jahrbuch für Geologie und Paläontologie*, *135*, 1–18.

Baud, P., Rolland, A., Heap, M., Xu, T., Nicolé, M., Ferrand, T., & Conil, N. (2016). Impact of stylolites on the mechanical strength of limestone. *Tectonophysics*, *690*, 4–20. https://doi.org/10.1016/j.tecto.2016.03.004

Baud, P., Schubnel, A., & Wong, T.-f. (2000). Dilatancy, compaction, and failure mode in Solnhofen limestone. *Journal of Geophysical Research: Solid Earth*, *105*(B8), 19289–19303. https://doi.org/10.1029/2000jb900133

Baud, P., Vinciguerra, S., David, C., Cavallo, A., Walker, E., & Reuschlé, T. (2009). Compaction and failure in high porosity carbonates: Mechanical data and microstructural observations. *Pure and Applied Geophysics*, *166*(5), 869–898. https://doi.org/10.1007/s00024-009-0493-2

Baud, P., Zhu, W., & Wong, T.-f. (2000). Failure mode and weakening effect of water on sandstone. *Journal of Geophysical Research: Solid Earth*, *105*(B7), 16371–16389. https://doi.org/10.1029/2000JB900087

Bestmann, M., & Prior, D. J. (2003). Intragranular dynamic recrystallization in naturally deformed calcite marble: Diffusion accommodated grain boundary sliding as a result of subgrain rotation recrystallization. *Journal of Structural Geology*, *25*(10), 1597–1613. https://doi.org/10.1016/S0191-8141(03)00006-3

Boulton, C., Niemeijer, A. R., Hollis, C. J., Townend, J., Raven, M. D., Kulhanek, D. K., & Shepherd, C. L. (2019). Temperature-dependent frictional properties of heterogeneous Hikurangi subduction zone input sediments, ODP site 1124. *Tectonophysics*, *757*, 123–139. https://doi.org/10.1016/j.tecto.2019.02.006

Brace, W. (1978). Volume changes during fracture and frictional sliding: A review. *Pure and Applied Geophysics*, *116*, 603–14. https://doi.org/10.1007/BF00876527

Brace, W., & Martin, R. (1968). A test of the law of effective stress for crystalline rocks of low porosity. *International Journal of Rock Mechanics and Mining Sciences & Geomechanics Abstracts*, *5*(5), 415–426. https://doi.org/10.1016/0148-9062(68)90045-4

Brantut, N., Heap, M. J., Baud, P., & Meredith, P. G. (2014). Mechanisms of time-dependent deformation in porous limestone. *Journal of Geophysical Research: Solid Earth*, *119*(7), 5444–5463. https://doi.org/10.1002/2014jb011186

Burnham, C. W., Holloway, J. R., & Davis, N. F. (1969). Thermodynamic properties of water to 1000°C and 10,000 bars. In *Thermodynamic properties of water to 1000°C and 10,000 bars*. Geological Society of America. https://doi.org/10.1130/SPE132-p1

Caciagli, N. C., & Manning, C. E. (2003). The solubility of calcite in water at 6–16 kbar and 500°C–800°C. *Contributions to Mineralogy and Petrology*, *146*(3), 275–285. https://doi.org/10.1007/s00410-003-0501-y

Carslaw, H., Jaeger, J., & Jaeger, J. (1959). *Conduction of heat in solids*. Clarendon Press. Retrieved from https://books.google.com/books?id=y20sAAAAYAAJ

Chandler, M. R., Meredith, P. G., Brantut, N., & Crawford, B. R. (2017). Effect of temperature on the fracture toughness of anisotropic shale and other rocks. *Geological Society, London, Special Publications*, *454*(1), 295–303. https://doi.org/10.1144/SP454.6

Curran, J. H., & Carroll, M. M. (1979). Shear stress enhancement of void compaction. *Journal of Geophysical Research: Solid Earth*, *84*(B3), 1105–1112. https://doi.org/10.1029/JB084iB03p01105

Dandekar, D. P. (1968). Variation in the elastic constants of calcite with temperature. *Journal of Applied Physics*, *39*(8), 3694–3699. https://doi.org/10.1063/1.1656842

Demurtas, M., Smith, S. A., Prior, D. J., Spagnuolo, E., & Di Toro, G. (2019). Development of crystallographic preferred orientation during cataclasis in low-temperature carbonate fault gouge. *Journal of Structural Geology*, *126*, 37–50. https://doi.org/10.1016/j.jsg.2019.04.015

den Brok, S. W. J. (1998). Effect of microcracking on pressure-solution strain rate: The Gratz grain-boundary model. *Geology*, *26*(10), 915–918. https://doi.org/10.1130/0091-7613(1998)026<0915:EOMOPS>2.3.CO;2

Dielforder, A., Vollstaedt, H., Vennemann, T., Berger, A., & Herwegh, M. (2015). Linking megathrust earthquakes to brittle deformation in a fossil accretionary complex. *Nature Communications*, *6*(1), 1–10. https://doi.org/10.1038/ncomms8504

Duda, M., & Renner, J. (2012). The weakening effect of water on the brittle failure strength of sandstone. *Geophysical Journal International*, *192*(3), 1091–1108. https://doi.org/10.1093/gji/ggs090

Edmond, J., & Paterson, M. (1972). Volume changes during the deformation of rocks at high pressures. *International Journal of Rock Mechanics and Mining Sciences & Geomechanics Abstracts*, *9*(2), 161–182. https://doi.org/10.1016/0148-9062(72)90019-8

Fischer, G., & Paterson, M. (1989). Dilatancy during rock deformation at high-temperatures and pressures. *Journal of Geophysical Research: Solid Earth*, *94*(B12), 17607–17617. https://doi.org/10.1029/JB094iB12p17607

Fischer, G., & Paterson, M. (1992). Chapter 9 measurement of permeability and storage capacity in rocks during deformation at high-temperature and pressure. In B. Evans, & T. f. Wong (Eds.), *Fault mechanics and transport properties of rocks* (Vol. 51, pp. 213–252). Academic Press. Retrieved from https://www.sciencedirect.com/science/article/pii/S0074614208628247

Fredrich, J. T., Evans, B., & Wong, T.-f. (1989). Micromechanics of the brittle to plastic transition in Carrara marble. *Journal of Geophysical Research: Solid Earth*, *94*(B4), 4129–4145. https://doi.org/10.1029/jb094ib04p04129

Fredrich, J. T., Evans, B., & Wong, T.-f. (1990). Effect of grain size on brittle and semi-brittle strength: Implications for micromechanical modeling of failure in compression. *Journal of Geophysical Research: Solid Earth*, *95*(B7), 10907–10920. https://doi.org/10.1029/JB095iB07p10907

French, M. E., & Condit, C. B. (2019). Slip partitioning along an idealized subduction plate boundary at deep slow slip conditions. *Earth and Planetary Science Letters*, *528*, 115828. https://doi.org/10.1016/j.epsl.2019.115828

French, M. E., & Zhu, W. (2017). Slow fault propagation in serpentinite under conditions of high pore fluid pressure. *Earth and Planetary Science Letters*, *473*, 131–140. https://doi.org/10.1016/j.epsl.2017.06.009

French, M. E., Zhu, W., Xiao, X., Evans, B., & Prior, D. J. (2021). Mechanical strength of water-saturated Solnhofen limestone at elevated temperatures, [Dataset]. https://doi.org/10.25611/0EMQ-H903

Frost, H., & Ashby, M. (1982). *Deformation-mechanism maps: The plasticity and creep of metals and ceramics*. Elsevier Science Limited. Retrieved from https://books.google.com/books?id=s9BRAAAAMAAJ

Ginder, R. S., Nix, W. D., & Pharr, G. M. (2018). A simple model for indentation creep. *Journal of the Mechanics and Physics of Solids*, *112*, 552–562. https://doi.org/10.1016/j.jmps.2018.01.001

Griggs, D. T., Turner, F. J., & Heard, H. C. (1960). Chapter 4: Deformation of rocks at 500°C–800°C. In *Rock deformation (A symposium)*. Geological Society of America. https://doi.org/10.1130/MEM79-p39

Hadizadeh, J., & Law, R. (1991). Water-weakening of sandstone and quartzite deformed at various stress and strain rates. *International Journal of Rock Mechanics and Mining Sciences & Geomechanics Abstracts*, *28*(5), 431–439. https://doi.org/10.1016/0148-9062(91)90081-v

Handin, J., & Hager, R. V. (1958). Experimental deformation of sedimentary rocks under confining pressure: Tests at high-temperature. *American Association of Petroleum Geologists Bulletin*, *42*(1), 2892–2934. https://doi.org/10.1306/0bda5c27-16bd-11d7-8645000102c1865d

Heard, H. C. (1960). Chapter 7: Transition from brittle fracture to ductile flow in Solenhofen limestone as a function of temperature, confining pressure, and interstitial fluid pressure. In *Rock deformation (A symposium)*. Geological Society of America. https://doi.org/10.1130/MEM79-p193

Higgs, N. G. (1981). *Mechanical properties of ultrafine quartz, chlorite, and bentonite in environments appropriate to upper-crustal earthquakes (Unpublished doctoral dissertation)*. Texas A&M Univeristy

Jefferd, M., Brantut, N., Meredith, P. G., Mitchell, T. M., & Plümper, O. (2021). Compactive deformation of sandstone under crustal pressure and temperature conditions. *Journal of Geophysical Research: Solid Earth*, *126*(4), e2020JB020202. https://doi.org/10.1029/2020JB020202

Leah, H., Fagereng, A., Meneghini, F., Morgan, J. K., Savage, H. M., Wang, M., & Ikari, M. J. (2020). Mixed brittle and viscous strain localization in pelagic sediments seaward of the Hikurangi margin, New Zealand. *Tectonics*, *39*(8), e2019TC005965. https://doi.org/10.1029/2019TC005965

Lisabeth, H. P., & Zhu, W. (2015). Effect of temperature and pore fluid on the strength of porous limestone. *Journal of Geophysical Research: Solid Earth*, *120*(9), 6191–6208. https://doi.org/10.1002/2015JB012152

Lloyd, G. E. (1985). Applications of electron microscopy in Earth sciences. In J. C. White (Ed.), *Mineralogical Association of Canada Short Course* (Vol. 11, pp. 158–188).

Mainprice, D., Hielscher, R., & Schaeben, H. (2011). Calculating anisotropic physical properties from texture data using the MTEX open-source package. *Geological Society, London, Special Publications*, *360*(1), 175–192. https://doi.org/10.1144/SP360.10

Munnecke, A., Westphal, H., & Kolbl-Ebert, M. (2008). Diagenesis of plattenkalk: Examples from the Solnhofen area (upper Jurassic, southern Germany). *Sedimentology*, *55*(6), 1931–1946. https://doi.org/10.1111/j.1365-3091.2008.00975.x

Nakashima, S. (1995). Diffusivity of ions in pore water as a quantitative basis for rock deformation rate estimates. *Tectonophysics*, *245*(3), 185–203. Influence of Fluids on Deformation Processes in Rocks https://doi.org/10.1016/0040-1951(94)00234-Z

Nicolas, A., Fortin, J., & Guéguen, Y. (2017). Micromechanical constitutive model for low-temperature constant strain rate deformation of limestones in the brittle and semi-brittle regime. *Geophysical Journal International*, *211*(1), 300–321. https://doi.org/10.1093/gji/ggx299

Nicolas, A., Fortin, J., Regnet, J., Dimanov, A., & Guéguen, Y. (2016). Brittle and semi-brittle behaviors of a carbonate rock: Influence of water and temperature. *Geophysical Journal International*, *206*(1), 438–456. https://doi.org/10.1093/gji/ggw154

Noël, C., Baud, P., & Violay, M. (2021). Effect of water on sandstone's fracture toughness and frictional parameters: Brittle strength constraints. *International Journal of Rock Mechanics and Mining Sciences*, *147*, 104916. https://doi.org/10.1016/j.ijrmms.2021.104916

Noël, C., Passelègue, F. X., & Violay, M. (2021). Brittle faulting of ductile rock induced by pore fluid pressure build-up. *Journal of Geophysical Research: Solid Earth*, *126*(3). https://doi.org/10.1029/2020JB021331

Ougier-Simonin, A., & Zhu, W. (2013). Effects of pore fluid pressure on slip behaviors: An experimental study. *Geophysical Research Letters*, *40*(11), 6pp. https://doi.org/10.1002/grl.50543

Plank, T., & Langmuir, C. H. (1998). The chemical composition of subducting sediment and its consequences for the crust and mantle. *Chemical Geology*, *145*(3), 325–394. https://doi.org/10.1016/S0009-2541(97)00150-2

Prior, D. J., Boyle, A. P., Brenker, F., Cheadle, M. C., Day, A., Lopez, G., et al. (1999). The application of electron backscatter diffraction and orientation contrast imaging in the SEM to textural problems in rocks. *American Mineralogist*, *84*(11–12), 1741–1759. https://doi.org/10.2138/am-1999-11-1204

Rabat, Ã., Cano, M., & Tomás, R. (2020). Effect of water saturation on strength and deformability of building calcarenite stones: Correlations with their physical properties. *Construction and Building Materials*, *232*, 117259. https://doi.org/10.1016/j.conbuildmat.2019.117259

Rabinowitz, H. S., Savage, H. M., Skarbek, R. M., Ikari, M. J., Carpenter, B. M., & Collettini, C. (2018). Frictional behavior of input sediments to the Hikurangi trench, New Zealand. *Geochemistry, Geophysics, Geosystems*, *19*(9), 2973–2990. https://doi.org/10.1029/2018GC007633

Rashid, F., Glover, P., Lorinczi, P., Hussein, D., Collier, R., & Lawrence, J. (2015). Permeability prediction in tight carbonate rocks using capillary pressure measurements. *Marine and Petroleum Geology*, *68*, 536–550. https://doi.org/10.1016/j.marpetgeo.2015.10.005

Renard, F., Ortoleva, P., & Gratier, J. P. (1997). Pressure solution in sandstones: Influence of clays and dependence on temperature and stress. *Tectonophysics*, *280*(3), 257–266. https://doi.org/10.1016/s0040-1951(97)00039-5

Renner, J., & Rummel, F. (1996). The effect of experimental and microstructural parameters on the transition from brittle failure to cataclastic flow of carbonate rocks. *Tectonophysics*, *258*(1), 151–169. https://doi.org/10.1016/0040-1951(95)00192-1

Røyne, A., Bisschop, J., & Dysthe, D. K. (2011). Experimental investigation of surface energy and subcritical crack growth in calcite. *Journal of Geophysical Research: Solid Earth*, *116*(B4). https://doi.org/10.1029/2010JB008033

Rudnicki, J., & Rice, J. (1975). Conditions for the localization of deformation in pressure-sensitive dilatant materials. *Journal of the Mechanics and Physics of Solids*, *23*(6), 371–394. https://doi.org/10.1016/0022-5096(75)90001-0

Rutter, E. H. (1972). The influence of interstitial water on the rheological behavior of calcite rocks. *Tectonophysics*, *14*(1), 13–33. https://doi.org/10.1016/0040-1951(72)90003-0

Rutter, E. H. (1974). The influence of temperature, strain rate, and interstitial water in the experimental deformation of calcite rocks. *Tectonophysics*, *22*(3), 311–334. https://doi.org/10.1016/0040-1951(74)90089-4

Rutter, E. H. (1986). On the nomenclature of mode of failure transitions in rocks. *Tectonophysics*, *122*(3), 381–387. https://doi.org/10.1016/0040-1951(86)90153-8

Rutter, E. H., & Elliott, D. (1976). The kinetics of rock deformation by pressure solution. *Philosophical Transactions of the Royal Society of London—Series A: Mathematical and Physical Sciences*, *283*(1312), 203–219. http://www.jstor.org/stable/74639

Rybacki, E., Niu, L., & Evans, B. (2021). Semi-brittle deformation of Carrara marble: Hardening and twinning induced plasticity. *Journal of Geophysical Research: Solid Earth*, *126*(12). https://doi.org/10.1029/2021JB022573

Schmitt, D. R., & Zoback, M. D. (1992). Diminished pore pressure in low-porosity crystalline rock under tensional failure: Apparent strengthening by dilatancy. *Journal of Geophysical Research: Solid Earth*, *97*(B1), 273–288. https://doi.org/10.1029/91JB02256

Schubnel, A., Fortin, J., Burlini, L., & Guéguen, Y. (2005). Damage and recovery of calcite rocks deformed in the cataclastic regime. *Geological Society, London, Special Publications*, *245*(1), 203–221. https://doi.org/10.1144/gsl.sp.2005.245.01.10

Segnit, E., Holland, H., & Biscardi, C. (1962). The solubility of calcite in aqueous solutions—I: The solubility of calcite in water between 75° and 200° at CO_2 pressures up to 60 atm. *Geochimica et Cosmochimica Acta*, *26*(12), 1301–1331. https://doi.org/10.1016/0016-7037(62)90057-1

Seward, G. G. E., Prior, D. J., Wheeler, J., Celotto, S., Halliday, D. J. M., Paden, R. S., & Tye, M. R. (2002). High-temperature electron backscatter diffraction and scanning electron microscopy imaging techniques: In situ investigations of dynamic processes. *Scanning*, *24*(5), 232–240. https://doi.org/10.1002/sca.4950240503

Sly, M. K., Thind, A. S., Mishra, R., Flores, K. M., & Skemer, P. (2019). Low-temperature rheology of calcite. *Geophysical Journal International*, *221*(1), 129–141. https://doi.org/10.1093/gji/ggz577

Turner, F. J., Griggs, D. T., & Heard, H. (1954). Experimental deformation of calcite crystals. *GSA Bulletin*, *65*(9), 883–934. https://doi.org/10.1130/0016-7606%281954%2965%5B883:edocc%5D2.0.co;2

Vajdova, V., Baud, P., & Wong, T.-f. (2004). Compaction, dilatancy, and failure in porous carbonate rocks. *Journal of Geophysical Research: Solid Earth*, *109*(B5). https://doi.org/10.1029/2003JB002508

Valcke, S. L. A., Pennock, G. M., Drury, M. R., & De Bresser, J. H. P. (2006). Electron backscattered diffraction as a tool to quantify subgrains in deformed calcite. *Journal of Microscopy*, *224*(3), 264–276. https://doi.org/10.1111/j.1365-2818.2006.01698.x

Verberne, B. A., Niemeijer, A. R., De Bresser, J. H. P., & Spiers, C. J. (2015). Mechanical behavior and microstructure of simulated calcite fault gouge sheared at 20°C–600°C: Implications for natural faults in limestones. *Journal of Geophysical Research: Solid Earth*, *120*(12), 8169–8196. https://doi.org/10.1002/2015JB012292

Verberne, B. A., Spiers, C. J., Niemeijer, A. R., De Bresser, J. H. P., De Winter, D. A. M., & Plümper, O. (2014). Frictional properties and microstructure of calcite-rich fault gouges sheared at sub-seismic sliding velocities. *Pure and Applied Geophysics*, *171*(10), 2617–2640. https://doi.org/10.1007/s00024-013-0760-0

Voigtländer, A., Leith, K., & Krautblatter, M. (2018). Subcritical crack growth and progressive failure in Carrara marble under wet and dry conditions. *Journal of Geophysical Research: Solid Earth*, *123*(5), 3780–3798. https://doi.org/10.1029/2017JB014956

Wang, X.-Q., Schubnel, A., Fortin, J., Guéguen, Y., & Ge, H.-K. (2013). Physical properties and brittle strength of thermally cracked granite under confinement. *Journal of Geophysical Research: Solid Earth*, *118*(12), 6099–6112. https://doi.org/10.1002/2013JB010340

Wong, T.-F., & Baud, P. (2012). The brittle-ductile transition in porous rock: A review. *Journal of Structural Geology*, *44*, 25–53. https://doi.org/10.1016/j.jsg.2012.07.010

Wong, T.-F., David, C., & Zhu, W. (1997). The transition from brittle faulting to cataclastic flow in porous sandstones: Mechanical deformation. *Journal of Geophysical Research: Solid Earth*, *102*(B2), 3009–3025. https://doi.org/10.1029/96JB03281

Zhang, X., Spiers, C. J., & Peach, C. J. (2010). Compaction creep of wet granular calcite by pressure solution at 28°C–150°C. *Journal of Geophysical Research: Solid Earth*, *115*(B9). https://doi.org/10.1029/2008JB005853

Zhao, Y., Zhang, L., Liao, J., Wang, W., Liu, Q., & Tang, L. (2020). Experimental study of fracture toughness and subcritical crack growth of three rocks under different environments. *International Journal of Geomechanics*, *20*(8), 04020128. https://doi.org/10.1061/(ASCE)GM.1943-5622.0001779